Copyright
by
Kevin David Anderson
2014

The Thesis Committee for Kevin David Anderson
certifies that this is the approved version of the following thesis

Nonradiative Decay of Singlet Excitons in Cadmium Selenide Nanoparticles

APPROVED BY

SUPERVISING COMMITTEE:

Peter J. Rossky, Supervisor

David Vanden Bout

Nonradiative Decay of Singlet Excitons in Cadmium Selenide Nanoparticles

by

Kevin David Anderson, B.S. Ch.

THESIS

Presented to the Faculty of the Graduate School of

The University of Texas at Austin

in Partial Fulfillment

of the Requirements

for the Degree of

MASTER OF ARTS

THE UNIVERSITY OF TEXAS AT AUSTIN

August 2014

Dedicated to my wife, Rebecca.

Acknowledgments

I wish to thank the multitudes of people who helped me. I wouldn't be where I am now without the support and patience of family, teachers, and friends. Special thanks to Dr. Eran Rabani, who provided immeasurable help and support over the course of this project.

Nonradiative Decay of Singlet Excitons in Cadmium Selenide Nanoparticles

Kevin David Anderson, M.A.
The University of Texas at Austin, 2014

Supervisor: Peter J. Rossky

Nonradiative decay of excitons is a competing process to Multi-Exciton Generation (MEG) in nanoparticles. Nonradiative decay of single excitons with sufficient energy to generate bi-excitons in $Cd_{20}Se_{19}$ and $Cd_{83}Se_{81}$ nanoparticles was studied using Tully's Molecular Dynamics with Quantum Transitions (MDQT) method and a CdSe pseudopotential. Exciton decay rates increase with increases in nanoparticle temperature and density of lower-lying excitonic states. There did not appear a significant effect of size on energy decay rates. The decay dynamics generally follow a gradual decay with transitions between nearby states. This is punctuated by periodic, short-lived periods of rapid downhill transitions that result in a large proportion of excess exciton energy being transferred to the vibrational motion of the nanoparticle. The time for relaxation to below the $2.0E_g$ cutoff was on the order of 1ps.

Table of Contents

List of Tables

List of Figures

Chapter 1

Introduction

The development of high efficiency light-harvesting devices has been an area of intense research interest [2,3]. However, there are several hurdles that these photochemical and photovoltaic devices must overcome. One such difficulty is the tuning of the absorption spectrum of the material to maximize overlap with the ambient solar spectrum. Another serious issue is the transport of charge carriers to the device's electrodes before carrier recombination can occur [4]. Finally, there is the issue of loss of energy from excitons with energy above that of the lowest lying exciton, known as "hot" excitons, which relax rapidly to the lowest lying excited state due to interaction with phonons [5]. These losses in the form of heat limit the maximum thermodynamic efficiency of a standard photovoltaic device to the Shockley-Queisser limit of approximately 32% [6].

One material that shows promise in improving photoconversion devices is that of semiconducting nanocrystals (NCs) [3, 7]. Such nanocrystal-based devices have been labelled third-generation photovoltaics [2,4]. These materials exhibit quantization effects due to the charge carriers (electrons and holes) being confined to regions of space that are less than the de Broglie wavelength of the carriers [2]. Nanocrystals that exhibit quantum confinement in all three spatial dimensions are referred to as *quantum dots*. NCs with quantum confinement in one or two dimensions are referred to quantum films and rods, respectively. The quantization effects allow for size-tuning optical properties of the nanocrystals, such as the band gap, and lead to interesting relaxation dynamics [7]. The relaxation dynamics of quantum dots and the rate of the losses of hot exciton excess energy as heat are the central

concern in this work.

The excess energy from hot carriers can be dissipated or converted in several ways. First, the carriers can separate and the excess energy can be captured by the system as increased chemical free energy or as increased electrical free energy at the device's electrodes. Second, a second electron-hole pair can be generated in a process akin to an inverse Auger recombination if the excess energy is greater than or equal to the band gap of the material. This is referred to as *multiple exciton generation*, or MEG [8]. MEG has also been observed in bulk semiconductors for some time, though the energy minimum energy associated with MEG is in the UV range, limiting functionality in photovoltaics [2]. It has been proposed that quantum confinement may enhance MEG in NCs. Finally, in an undesired fashion, the excess energy can be dissipated as heat via carrier-phonon interactions. This process can be slower in QDs than in bulk due to the so-called "phonon bottleneck", where the quantum confinement puts a larger gap between electronic states than a single phonon can absorb. Large gains in photoconversion devices can be gained if the first two paths dominate over the last path [2]. The prospect of such gains in photovoltaic efficiency has made MEG in semiconducting nanocrystals a very active area of research [2, 3, 9].

Multiple exciton generation has been reported in PbSe, PbS, PbTe, InAs, Si, and CdSe semiconductor nanocrystals and had been the focus of intense study [9]. This work will be centered on CdSe quantum dots. Several groups, including Rabani, Franceschetti, and Prezdho, have been modelling multiple exciton generation rates in these CdSe QDs [5,8–10]. Prezdho has been modelling the nonadiabatic relaxation of Cd_6Se_6 nanoparticles using time-domain *ab initio* methods [11]. While this level of theory accurately models individual states, it is computationally infeasible to apply it to the large manifold of relevant excitonic states in larger clusters since the density of states increases with particle size. It is important to understand the rate of nonradiative decay in these nanocrystals at these relevant energies

because it is a process that directly competes with MEG. If the nonradiative relaxation rate exceeds the MEG rate, MEG will not have a significant impact on photovoltaic efficiencies [8]. To this end, here, the nonadiabatic dynamics of singlet excitons at energies in excess of twice the band gap, the minimum required for MEG, in CdSe nanopartices are modeled using a pseudopotential state description for the electronic structure [8, 12] and Tully's "surface hopping with fewest switches" algorithm to simulate the dynamics of the system [13].

This report is organized as follows: First, the model used to simulate the CdSe nanoparticles will be described. Next, the surface hopping method will be outlined. A description of the procedure follows. In the next chapter the results of the simulations will be presented and discussed. Appendices providing detailed information about the derivation of coupling elements and supplemental figures can be found at the end of the report.

Chapter 2

Methods

In order to simulate the nonradiative decay of excitons in CdSe nanoparticles at energies relevant for MEG, Tully's Molecular Dynamics with Quantum Transitions (MDQT) method was used [13, 14]. In the first subsection, the electronic structure model will be described. Next, the MDQT method will be outlined. In the third subsection, the procedure used for simulating exciton relaxation will be outlined.

2.1 Model Description

The CdSe nanoparticles studied were prepared using the method described in Reference [15]. The nanoparticles are quasi-spherical and consist of a wurtzite crystal structure. All Cadmium and Selenide ions have no more than two dangling bonds. The nanoparticles were capped with trioctylphosphine oxide (TOPO) to stabilize the surface and prevent aggregation [7, 15]. However, the effects of surface passivation were not considered in this study, as in related previous work [11], beyond the generation of initial atomic configuration. Since the phosphine oxide-Cd interaction is weak, the ability of the capping layer to dissipate heat is not an important omission [7]. Specifically, two configurations, $Cd_{20}Se_{19}$ and $Cd_{83}Se_{81}$, were modeled. Basic information about these nanoparticles can be found in Table 2.1. Although the model is quite simple, larger nanoparticles require a large amount of computer memory to model with this method, at least if implemented in a direct manner.

In order to study nonadiabatic dynamics for a large number of possible exciton states, several approximations were made. First, a semi-classical approximation was made

Cluster	Band gap(eV)	Dot Radius(nm)	Structure
$Cd_{20}Se_{19}$	3.80	1.19	Wurtzite
$Cd_{83}Se_{81}$	2.93	2.05	Wurtzite

Table 2.1: Basic information on studied nanoparticles.

to separate the classical and quantum coordinates. The quantum coordinates include the excited electron and the corresponding hole. The nuclear coordinates of the system are treated classically. The energy of the system is defined as

$$E^{total}(\mathbf{r}, \mathbf{R}) = E^{q}(\mathbf{r}; \mathbf{R}) + E^{c}(\mathbf{R}), \tag{2.1}$$

where $\mathbf{r}$ is the set of quantum coordinates and $\mathbf{R}$ is the set of classical coordinates [16], namely, the nuclear coordinates.

2.1.1 Quantum Subsystem

To generate the real-space single-particle pseudo-wavefunctions, a screened Hartree-Fock Hamiltonian is approximated by a pseudopotential that was parameterized using the experimentally determined bulk band structure. The full procedure for this process can be found in Ref. [12]. The general form of the exact quantum Hamiltonian takes the form of

$$H^{q} = \sum_{i} h_1 + \sum_{i} \sum_{j>i} W_2 \tag{2.2}$$

where h_1 is a one-body Hamiltonian

$$h_1(\mathbf{x}_1) = -\frac{1}{2}\nabla^2 - \sum_{\alpha} \frac{Z_\alpha}{r_{1\alpha}}, \tag{2.3}$$

W_2 is two-body potential

$$W_2(\mathbf{x}_1, \mathbf{x}_2) = \frac{1}{r_{12}^2}, \tag{2.4}$$

and the sum indices i and j run over all relevant electron pairs. Here, $\mathbf{x}_1$ is the collection of spatial and spin coordinates for electron 1, and α runs over all atomic centers. A Hartree-

Fock approximation is made, resulting in a screened one-body Hamiltonian, H_1.

$$H_1 = h_1 + J - K \tag{2.5}$$

where J and K are the standard one-electron coulomb and exchange terms, respectively [17]. The quantum Hamiltonian then becomes

$$H^q = \sum_i H_i + \sum_i \sum_{i<j} (W_{ij} - (J_{ij} - K_{ij})) = \sum_i H_i + \sum_i \sum_{j>i} U \tag{2.6}$$

where U is a perturbation consisting of the two-electron repulsion term minus the contribution of the one-electron Hartree-Fock coulomb and exchange terms already accounted for in H_1. In order to solve for the basis wavefuctions, H_1 is approximated using a semi-empirical pseudopotential:

$$H_1 \approx -\frac{1}{2}\nabla^2_{\mathbf{r}_1} - \sum_\alpha v_\alpha(\mathbf{r}_1 - \mathbf{R}_\alpha) \tag{2.7}$$

where H_1 is the pseudopotential-approximated one-electron Hamiltonian, $v_\alpha(\mathbf{r} - \mathbf{R}_\alpha)$ is the empirical pseudopotential for atom α, and $\mathbf{R}_\alpha$ is the position of atom type α. These pseudopotentials were previously fitted to reproduce the CdSe bulk band gap by Rabani and co-workers and are defined in Ref [12]. The resulting single particle Schrödinger equation,

$$H_i\theta_i = \epsilon_i\theta_i \tag{2.8}$$

where H_i is H_1 for particle i and ϵ_i is the energy of the single-particle basis function θ_i [12], was solved in real space by the filter diagonalization technique [18] for all occupied states and states up to $5.0E_g$ above the Fermi energy level. We define the unit E_g as the energy associated with the nanoparticle band gap. The generation of these single particle wavefunctions was carried out by Rabani.

In order to describe excitonic states, we first define the ground state wavefunction as

$$|\psi_{ground}\rangle = \left|\chi_1\chi_{\overline{1}}\cdots\chi_{occ}\chi_{\overline{occ}}\cdots\chi_{Fermi}\chi_{\overline{Fermi}}\right\rangle, \tag{2.9}$$

where *occ* denotes some occupied state, *Fermi* is the highest occupied orbital and χ is a spin-orbital. The spin orbital χ is defined as

$$\chi_i(\mathbf{x}_1) = \theta_i(\mathbf{r}_1)\alpha(\omega_1) \tag{2.10a}$$

$$\chi_{\bar{i}}(\mathbf{x}_1) = \theta_i(\mathbf{r}_1)\beta(\omega_1) \tag{2.10b}$$

where $\mathbf{r}_1$ is the collection of spatial coordinates of electron 1, and ω_1 is the spin coordinate of electron 1. The spin function α corresponds to a spin of $+\frac{1}{2}$ and β corresponds to a spin of $-\frac{1}{2}$. An excitonic state will be denoted as

$$|\psi_{occ}^{ex}\rangle = \left|\chi_1\chi_{\bar{1}}\cdots\chi_{ex}\chi_{\overline{occ}}\cdots\chi_{Fermi}\chi_{\overline{Fermi}}\right\rangle \tag{2.11}$$

where the excited electron has been excited from the *occ* occupied spin-orbital to the *ex* excited spin-orbital. The modeled excitons are in a *singlet* state. An excitation from *occ* to orbital *ex* can occur from either *occ* or $\overline{occ}$ as in the below equation

$$|\psi_{occ}^{ex}\rangle = \left|\chi_1\chi_{\bar{1}}\cdots\chi_{ex}\chi_{\overline{occ}}\cdots\chi_{Fermi}\chi_{\overline{Fermi}}\right\rangle \tag{2.12a}$$

$$|\psi_{\overline{occ}}^{\overline{ex}}\rangle = \left|\chi_1\chi_{\bar{1}}\cdots\chi_{occ}\chi_{\overline{ex}}\cdots\chi_{Fermi}\chi_{\overline{Fermi}}\right\rangle. \tag{2.12b}$$

In fact, neither situation results in a pure spin state if written as a single determinant [17]. Instead, we need a mixture of the two determinants as

$$|^s\psi_{occ}^{ex}\rangle = \frac{1}{\sqrt{2}}\left(|\psi_{\overline{occ}}^{\overline{ex}}\rangle + |\psi_{occ}^{ex}\rangle\right). \tag{2.13}$$

The ground state energy, E_{ground}, is the standard form

$$E(\mathbf{r};\mathbf{R}) = \langle\psi_{ground}(\mathbf{r};\mathbf{R})|H^q(\mathbf{r};\mathbf{R})|\psi_{ground}(\mathbf{r};\mathbf{R})\rangle. \tag{2.14}$$

The parametric dependence on $\mathbf{R}$ in (2.14) is a result of taking the Born-Oppenheimer approximation. We define the exciton energy as the difference between the excited electron and the corresponding hole state relative to the energy of the ground state. The set of exciton states simulated was selected based on the energies of the excitonic states relative to the band gap energy.

2.1.2 Classical Subsystem

The classical energy, E^c, is written as

$$E^c(\mathbf{R}) = \sum_{i=1}^{N} \frac{M_i \dot{\mathbf{R}}_i^2}{2} + V^c(\mathbf{R}), \tag{2.15}$$

where M_i is the mass of nucleus i, V^c is the classical potential energy surface, and N is the number of Cd and Se nuclei in the nanoparticle. V^c in this case is

$$V^c = \sum_{\alpha} \sum_{\beta>\alpha} V^c_{\alpha\beta} \tag{2.16}$$

where

$$V^c_{\alpha\beta} = \frac{q_\alpha q_\beta}{r_{\alpha\beta}} + 4\epsilon_{\alpha\beta}\left[\left(\frac{\sigma_{\alpha\beta}}{r_{\alpha\beta}}\right)^6 - \left(\frac{\sigma_{\alpha\beta}}{r_{\alpha\beta}}\right)^{12}\right], \tag{2.17}$$

σ is the radius of the potential well, ϵ is the well depth, $r_{\alpha\beta}$ refers to the distance between atoms α and β. The interatomic pair potentials for CdSe, $V^c_{\alpha\beta}$, are defined in Reference [1]. The values of the parameters can be found in Table 2.2. The Lorentz-Berthelot combining rules are used to find σ and ϵ for Cd-Se pairings, as shown below [1]:

$$\sigma_{Cd-Se} = \frac{\sigma_{Cd} + \sigma_{Se}}{2} \tag{2.18a}$$

$$\epsilon_{Cd-Se} = \sqrt{\epsilon_{Cd}\epsilon_{Se}}. \tag{2.18b}$$

The classical coordinates $\mathbf{R}$ evolve according to the following equation of motion.

$$M\ddot{\mathbf{R}} = \mathbf{F}^c = -\nabla_{\mathbf{R}} V^c(\mathbf{R}). \tag{2.19}$$

Generally speaking, there is an electronic $F^q = -\nabla_{\mathbf{R}}\langle\psi(\mathbf{r};\mathbf{R})|H^q(\mathbf{r};\mathbf{R})|\psi(\mathbf{r};\mathbf{R})\rangle$ contribution to the force. However, the effect of a single electron excitation delocalized over the nanoparticle is taken to have a negligibly small effect on the potential energy surface of the nuclear subsystem. The quantum subsystem will only affect the classical coordinates via momentum boosts during electronic transitions. This aspect will be discussed in detail below.

atom	$q(e^-)$	$\sigma(\mathring{A})$	$\epsilon(K)$
Cd	1.18	1.98	16.8
Se	-1.18	5.24	14.9

Table 2.2: Potential energy parameter values [1].

2.2 Surface Hopping Method

As mentioned previously, Tully's MDQT was used to simulate the exciton dynamics in our model system [13]. The quantum subsystem evolves in time according to the standard time-dependent Schrödinger equation

$$i\hbar\frac{\partial\psi(\mathbf{r},t;\mathbf{R})}{\partial t} = H^q(\mathbf{r};\mathbf{R})\psi(\mathbf{r},t;\mathbf{R}). \tag{2.20}$$

In principle, the basis set can be any set of orthonormal basis functions [13]. In this surface hopping algorithm, the *primary* wavefunction, ψ, is propagated continuously in time. The primary wavefunction is given as:

$$\psi(\mathbf{r},t;\mathbf{R}) = \sum_i c_i(t)\phi_i(\mathbf{r};\mathbf{R}(t)), \tag{2.21}$$

where we assume that atomic motion can be described by some classical trajectory, which is undetermined at this point, so that $\mathbf{R} = \mathbf{R}(t)$. The Hamiltonian $H^q(\mathbf{r};\mathbf{R})$ then becomes time dependent through its dependence on $\mathbf{R}(t)$. In the above equation, ϕ_i are the excitonic basis wavefunctions defined in equation 2.13. The sum index i runs over all relevant singlet excitonic states such that

$$|\phi_i\rangle = |^s\psi^{ex}_{occ}\rangle. \tag{2.22}$$

Here, the s superscript denotes a singlet state as defined by equation 2.13 and the index i corresponds to a unique combination of occupied *occ* and excited *ex* states. The determination of relevant states is discussed in Section 2.3. Substituting (2.21) into (2.20), multiplying by $\langle\phi_j|$, integrating over $\mathbf{r}$, and dividing by $i\hbar$ yields

$$\dot{c}_k = -\sum_j c_j\left(\frac{i}{\hbar}V_{kj} + \dot{\mathbf{R}}(t)\cdot\mathbf{d}_{kj}\right), \tag{2.23}$$

where

$$V_{ij} = \langle \phi_i(\mathbf{r}; \mathbf{R}(t)) | H^q(\mathbf{r}, \mathbf{R}(t)) | \phi_j(\mathbf{r}; \mathbf{R}(t)) \rangle \tag{2.24}$$

and

$$\mathbf{d}_{ij} = \langle \phi_i(\mathbf{r}; \mathbf{R}(t)) | \nabla_{\mathbf{R}} \phi_j(\mathbf{r}; \mathbf{R}(t)) \rangle \tag{2.25}$$

where, as usual, only the off-diagonal terms of $\mathbf{d}_{ij}$ are non-zero and V_{ij} generally includes coulomb and exchange terms. As previously discussed, the wavefunctions are singlet states.

Our basis functions do not have an explicit dependence on time. Instead, they depend parametrically on the nuclear coordinates $\mathbf{R}$, which do have a time dependence. Therefore, the derivative of the basis functions with respect to time must employ the chain rule as follows

$$\left| \frac{\partial \phi_j(\mathbf{r}; \mathbf{R}(t))}{\partial t} \right\rangle = \left| \frac{\partial \phi_j(\mathbf{r}; \mathbf{R}(t))}{\partial \mathbf{R}} \right\rangle \cdot \frac{\partial \mathbf{R}(t)}{\partial t} = \dot{\mathbf{R}}(t) \cdot \nabla_{\mathbf{R}} \left| \phi_j \left(\mathbf{r}; \mathbf{R}(t) \right) \right\rangle . \tag{2.26}$$

Multiplication of equation 2.26 by $\langle {}^s\psi_k(\mathbf{r}; \mathbf{R}(t))|$ and using equation 2.25, we obtain

$$\left\langle \phi_k(\mathbf{r}; \mathbf{R}(t)) \right| \frac{\partial \phi_j(\mathbf{r}; \mathbf{R}(t))}{\partial t} \right\rangle = \dot{\mathbf{R}}(t) \cdot \mathbf{d}_{kj}. \tag{2.27}$$

We neglect the effect of nuclear fluctuations on H^q and $|{}^s\psi^{ex}_{occ}\rangle$. The thermal fluctuations of the nuclear positions are small compared to the size of the entire nanoparticle while the excitonic wavefunctions are largely delocalized. By extension, $\mathbf{d}_{ij}$, and V_{ij} become time-independent as well. The use of this approximation facilitates the calculation of exciton dynamics of the nanoparticles because it is unnecessary to solve the Schrödinger wave equation at later time steps. Additionally, the coupling elements do not need to be recalculated. With this approximation, the quantum and classical subsystems are only coupled through the classical trajectory $\mathbf{R}(t)$.

It is worth noting that because these $|\phi_i\rangle$ states are singlet exciton states for a specific electron/hole pair, the elements of V_{ij} and $\mathbf{d}_{ij}$ are evaluated using equation 2.13.

Looking at the electron and hole components of our basis functions as $|\phi_i\rangle = |^s\psi_a^r\rangle$ and $|\phi_j\rangle = |^s\psi_b^s\rangle$ (equation 2.12) , the off-diagonal elements in equation 2.24 become

$$(V_{ij})_{(a\neq b \text{ and } r\neq s)} = 2(v_{arbs}) - v_{absr} \tag{2.28}$$

$$(V_{ij})_{(a\neq b, r=s \text{ or } r\neq s, a=b)} = v_{arbs} \tag{2.29}$$

where v_{arbs} is the coulomb integral, v_{absr} is the exchange integral, and the integral notation is as follows

$$v_{arbs} = \int\int \chi_a^*(\mathbf{x}_1)\chi_r(\mathbf{x}_1)\frac{1}{r_{12}}\chi_b^*(\mathbf{x}_2)\chi_s(\mathbf{x}_2)d\mathbf{x}_1 d\mathbf{x}_2. \tag{2.30}$$

The diagonal components in equation 2.24 are simply the associated energy eigenvalues. The off diagonals are essentially $\langle^s\psi_a^r|U|^s\psi_b^s\rangle$, where U is defined in equation 2.6.

In order to calculate the nonadiabatic coupling vectors $\mathbf{d}_{ij}$ in equation 2.25, the Hellmann-Feynman expression is used [14]. Taking the gradient of the quantum Hamiltonian element between states i and j with respect to $\mathbf{R}$, we obtain

$$\nabla_{\mathbf{R}}\left[\langle\phi_i|H_1|\phi_j\rangle\right] = \langle\phi_i|\nabla_{\mathbf{R}}H_1|\phi_j\rangle + \langle\nabla_{\mathbf{R}}\phi_i|H_1|\phi_j\rangle + \langle\phi_i|H_1|\nabla_{\mathbf{R}}\phi_j\rangle = 0. \tag{2.31}$$

The basis functions are eigenvectors of H_1, so above equation becomes

$$\nabla_{\mathbf{R}}\left[\langle\phi_i|H_1|\phi_j\rangle\right] = \langle\phi_i|\nabla_{\mathbf{R}}H_1|\phi_j\rangle - \left[\epsilon_j - \epsilon_i\right]\langle\phi_i|\nabla_{\mathbf{R}}\phi_j\rangle = 0, \tag{2.32}$$

where ϵ_j is the energy of single particle state j. The the only term within H_1 that depends on $\mathbf{R}$ is the pseudopotential term v_α. Equation 2.32 can then be rearranged as

$$\langle\phi_i(\mathbf{r};\mathbf{R})|\nabla_{\mathbf{R}}\phi_j(\mathbf{r};\mathbf{R})\rangle = \mathbf{d}_{ij} = \sum_\alpha \frac{\langle\phi_i|\nabla_{\mathbf{R}}v_\alpha(\mathbf{r}-\mathbf{R}_\alpha)|\phi_j\rangle}{\epsilon_j - \epsilon_i}. \tag{2.33}$$

As the *primary* wavefunction evolves continuously, the MDQT *reference* wavefunction remains resolved in one of the basis functions and will periodically make a discrete, instantaneous *hop* from $\phi_i \rightarrow \phi_j$.

These sudden transitions between states is a feature of surface hopping algorithms. Tully's "fewest switches" algorithm also results in sudden transitions in regions of coupling. However, a swarm of trajectories will result in a flow of flux from one state to another within regions of coupling between states [13] because different trajectories within the swarm make the transitions at different times. It does so with a minimum number of quantum hops per time step. The probability of switching from current state i to another state j in the interval $t \rightarrow (t + \Delta t)$ is

$$g_{ij} = \frac{b_{ji}(t + \Delta t)\Delta t}{a_{ii}(t + \Delta t)}, \tag{2.34}$$

where

$$a_{ij} \equiv c_i c_j^*, \tag{2.35}$$

a_{ii} is the population in state i, and

$$b_{ji} \equiv \frac{2}{\hbar} Im(a^* V_{kl}) - 2Re(a_{ji}^* \dot{\mathbf{R}}(t) \cdot \mathbf{d}_{ji}). \tag{2.36}$$

In the present case, our pseudopotential-based basis is an approximate adiabatic basis, and the off-diagonal elements V_{ij} only serve to correct this approximation. Hence, "hops" that might be induced by V_{ij} would be unphysical and energy differences can not be coupled to the nuclear coordinates. Since we are in a nonadiabatic scheme, there is no mechanism for energy conservation. In this case, we use the coulomb coupling, V_{ij}, only in the propagation (Eq. 2.23). The V_{ij} terms indirectly, then, affect the hopping between excitonic states. The hopping probability is then computed using the nonadiabatic coupling with

$$b_{ji} = -2Re(a_{ji}^* \dot{\mathbf{R}}(t) \cdot \mathbf{d}_{ji}) \tag{2.37}$$

In this algorithm, if $g_{i \rightarrow j}$ is less than zero, then it is reset to zero [14]. It also needs to be noted that Δt must be chosen such that the populations do not significantly change

within the interval. That is,

$$a_{ii}(t + \Delta t) - a_{ii}(t) \approx \dot{a_{ii}} \Delta t. \tag{2.38}$$

Because of the extreme separation of quantum and classical coordinate time scales in this system, the quantum coordinates should be integrated by a much smaller time interval δ than the classical system; we use $\delta t / \partial t = 200$. This allows for accurate integration of the quantum coordinates [13, 14]. Additionally, the Condon approximation is in use. Due to the separation in time scales, the transitions are taken to be instantaneous with respect to the nuclear coordinates.

In order to select from the possible hops with the proper probability weightings, a random number with a uniform distribution over $(0, 1)$, ζ, is chosen. The different switching probabilities are then ordered along the range [0,1]. A hop from state $1 \rightarrow 4$ would occur if $g_{1,2} + g_{1,3} < \zeta < g_{1,4}$. Should the sum of the calculated switching probabilities be greater than 1 due to the linear approximation in equation 2.38, the values are renormalized such that the total probability equals 1 [14].

Should a hop be successfully selected, the energy transfer between the quantum and classical subsystems occurs in the direction of the nonadiabatic coupling with velocity rescaling such that energy is conserved [13]. If $\Delta E^q > 0$ ("upwards" hop), the nuclear velocities must be checked to ensure that there is enough kinetic energy parallel to the $\mathbf{d}_{ij}$ vector to supply this energy. If this is not the case, the hop is rejected and the classical velocities reverse in the direction of the nonadiabatic coupling [14]. Specifically, the new velocities resulting from a switch from singlet exciton state i to state j, $\dot{\mathbf{R}}^{new}$, can be found to be

$$\dot{\mathbf{R}}_{\alpha}^{new} = \dot{\mathbf{R}}_{\alpha} - \gamma_{ij} \frac{\mathbf{d}_{ij}^{\alpha}}{m_{\alpha}}, \tag{2.39}$$

where $\mathbf{d}_{ij}^{\alpha}$ is the nonadiabatic coupling vector associated with atom α,

$$\gamma_{ij} = \frac{b_{ij} \pm \sqrt{b_{ij}^2 + 4a_{ij}[\epsilon_i - \epsilon_j]}}{2a_{ij}}, \tag{2.40}$$

$$a_{ij} = \frac{1}{2} \sum_{\alpha} \frac{|\mathbf{d}_{ij}|^2}{m_{\alpha}}, \tag{2.41}$$

and

$$b_{ij} = \sum_{\alpha}^{N} \dot{\mathbf{R}}_{\alpha} \cdot \mathbf{d}_{ij}. \tag{2.42}$$

Addition applies in equation 2.40 when $b_{jk} < 0$, otherwise it is subtraction. Note, that the transition only occurs if $b_{ij}^2 + 4a_{ij}[\epsilon_i(\mathbf{R}) - \epsilon_j(\mathbf{R})] \geq 0$. If this is not the case, the hop is rejected and $\gamma_{ij} = b_{ij}/a_{ij}$. This new value of γ serves to reverse the velocity along $\mathbf{d}_{ij}$ [14].

All hops in this scheme are dictated directly by the amplitudes in the primary wavefunction and the nonadiabatic coupling elements between initial and final states. Therefore (see Appendix A), only electron or hole hops are possible, and not both in a single time step δt.

2.3 Procedure Outline

Step 1. Several ranges of initial excitation energy are chosen for each nanoparticle configuration based on the size of nanoparticle's band gap. MEG is no longer possible for excitons with less than $2.0E_g$ of excitation energy. Therefore, in this application, we do not consider excitons with initial excitation energies of less than $2.0E_g$ and simulations are terminated upon exciton decay below this energy [2,8]. Within our framework, all excitonic states that correspond to an electron and hole pair that differ in energy by less than $2.0E_g$ are considered to be cutoff states. Both computational expense and the lack of relevance of very high energy excitons in solar cell applications play a role in determining the upper limit of excitation energies. In general, the possible initial exciton states were sorted into

bins of $0.1E_g$ width. For $Cd_{20}Se_{19}$, bins were centered at $3.0E_g$, $3.5E_g$, and $4.0E_g$. For $Cd_{83}Se_{81}$, $2.5E_g$ and $2.8E_g$ bins were used. The upper bound on the exciton basis was set by adding a $0.05E_g$ buffer above the initial energy. The larger size and corresponding higher density of states made calculations at higher energy levels quite time consuming. There are around 16,000 possible exciton states in the 1.5-$4.0E_g$ range for $Cd_{20}Se_{19}$, and about 55,000 possible exciton states in the 1.5-$3.5E_g$ range for $Cd_{83}Se_{81}$. Moreover, the number of electron-electron interactions grows as the number of relevant exciton states squared. Within each bin, the different exciton states were ordered from highest to lowest oscillator strength. This was done because a higher oscillator strength corresponds to a stronger adsorption [17]. For each group, the 30 brightest excitonic states within $\pm 0.5E_g$ of the target energy were chosen in order to get reasonably smooth averages. The $3.0E_g$ group for $Cd_{83}Se_{81}$ contains an extra 10 trajectories because these were the smallest simulations and were performed first. It was later determined that the extra trajectories did not provide significant extra information, so they were omitted in the other groups. These states are treated as singlets as defined by equation 2.13.

Step 2. Because the input configurations for $Cd_{20}Se_{19}$ or $Cd_{83}Se_{81}$ were generated with the inclusion of surface-ligand potentials that are ignored in the study [15], it is necessary to optimize the nanoparticle configuration. This is achieved by integrating the classical equations of motion with periodic quenching of the nuclear velocities until a minimized configuration is achieved. Once the configuration is minimized, the system is equilibriated at 300K using Boltzmann sampling every 10 fs for 500 fs.

Step 3. Normal time evolution of the simulation begins. First, the classical coordinates are integrated in time from t to $(t + \Delta t)$ using the velocity-verlet algorithm and using a Δt of 1.0 fs [19].

Step 4. The quantum coordinates are integrated from t to $(t+\Delta t)$ using the Runge-

Kutta-Gill 4^{th} order algorithm [19]. This integration is carried out over many smaller substeps in order to maintain accurate integration across the multitude of electronic states. In this case, $\delta t = \Delta t/200$ [14].

Step 5. The probabilities for the reference state to make a hop are generated using equation 2.34. A pseudorandom number with a uniform distribution across $(0, 1)$ is generated and compared with the switching probabilities in the manner discussed above [14].

Step 6. If no hop is selected, the procedure repeats from Step 3. If a hop is selected, the velocity must be rescaled according to equation 2.40 and the above procedure.

Step 7. A check is made to see if the exciton has decayed to below the aforementioned $2.0E_g$ threshold. If this condition has been met, the trajectory is terminated. Otherwise, the procedure returns to Step 3 and continues.

Chapter 3

Results and Discussion

In this section, we describe the results of the simulations discussed in the previous section. Analysis includes first a discussion of the overall rate of exciton energy loss followed by a discussion of the dynamics of this exciton decay. The trajectory groups and number of trajectories in each group can be found in Table 3.1.

The average electronic trajectories and cluster temperatures for the groups of exciton trajectories for $Cd_{20}Se_{19}$ and $Cd_{83}Se_{81}$ discussed in the previous section can be seen in Figure 3.1. The temperature increase seen in this figure is a direct result of the energy transfer from the exciton to the classical atomic coordinates via the nonadiabatic couplings. This increase is more pronounced in $Cd_{20}Se_{19}$ than in $Cd_{83}Se_{81}$ due to both an increased amount of initial energy to transfer and a fewer number of atomic coordinates to accept the energy. The average electronic trajectory curves in Figure 3.1 is the average of all individual electronic trajectories with an exciton energy greater than twice the band gap within that particular cohort of trajectories. This method of averaging, while useful for tracking the

Nanoparticle	Starting energy	Number of Trajectories
$Cd_{83}Se_{81}$	$2.5E_g$	30
	$2.8E_g$	30
$Cd_{20}Se_{19}$	$3.0E_g$	40
	$3.5E_g$	30
	$4.0E_g$	30

Table 3.1: Trajectory groups. All trajectories within each group are the brightest states located within $\pm 0.05E_g$ of the listed starting energy.

overall rate of decay, does become more weighted toward the surviving trajectories at longer times. For this reason, Figure 3.1 is cut off at 700fs to mitigate this issue.

For a more detailed look at the data, the full electronic trajectories for $Cd_{20}Se_{19}$ can be found in Figures B.1 and B.2. The corresponding plots for $Cd_{83}Se_{81}$ can similarly be found in Figures B.3 and B.4. In these figures, some of the excitons failed to decay below the $2.0E_g$ threshold before the simulation hit its wall-clock time. It was determined that since the behaviour of trajectories appear to be consistent across the range of initial exciton energies studied for this cluster, additional resources would not be used on these simulations.

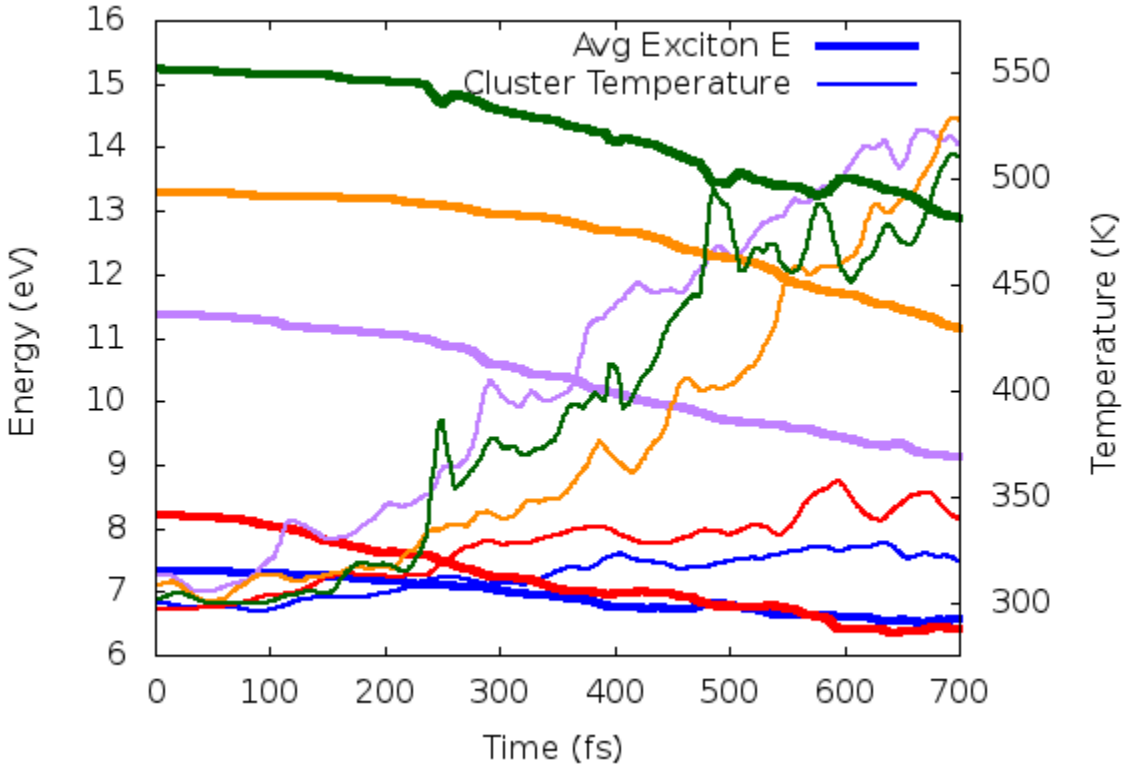

Figure 3.1: Average electronic energy (thick lines) and nanoparticle temperature (thin lines) vs time. Green, orange, and violet corresponds to $Cd_{20}Se_{19}$ trajectory cohorts starting at $4.0E_g$, $3.5E_g$, and $3.0E_g$, respectively. Red and blue curves correspond to $Cd_{83}Se_{81}$ trajectories starting at $2.8E_g$, and $2.5E_g$.

3.1 Rate of Exciton Energy Loss

As can be seen in Figure 3.1, the rate of exciton energy loss to the atomic nuclei is generally consistent across all of the $Cd_{20}Se_{19}$ cohorts and the group of $Cd_{83}Se_{81}$ trajectories with a $2.8E_g$ (8.2eV) initial exciton energy. The lone exception to the otherwise consistent slope of exciton energy loss occurs with lowest energy group, corresponding to $Cd_{83}Se_{81}$ with an initial exciton energy of $2.5E_g$ (7.325eV). This cohort has a slower rate of exciton decay than the other sets of trajectories. However, it should be noted that the average energy loss of the $2.8E_g$ initial exciton energy cohort slows and converges with the rate of the $2.5E_g$ initial exciton energy cohort as it approaches the sub-$2.5E_g$ energy range (Figure 3.2). This difference in electronic energy loss lies in the lower density of states found in the sub-$2.5E_g$ energy range, which can be seen in Figure 3.3.

A similar effect can be seen with the lowest energy cohort of $Cd_{20}Se_{19}$ in Figure 3.1. The average rate of decay decreases as the number of lower-laying states decreases. Figure 3.4 shows that the number of $Cd_{20}Se_{19}$ exciton states below a given energy level increases much more rapidly above approximately the 2.5-2.7E_g range. This trend is the same for $Cd_{83}Se_{81}$, though with a much larger total number of states.

In summary, the average exciton energy loss per unit time is qualitatively the same across all cohorts that have a suitably high number of lower-lying states. It is particularly interesting that this trend generally holds true even between cluster sizes. The lower density of states in $Cd_{20}Se_{19}$ than in $Cd_{83}Se_{81}$ is apparently offset by the increased heating observed in $Cd_{20}Se_{19}$; this stronger increase in velocities increase nonadiabatic coupling terms (equation 2.26). Further evidence of this temperature effect on the rate of exciton decay can be seen in Figure 3.1, where the $2.8E_g$ cohort of $Cd_{83}Se_{81}$ trajectories penetrates deeper into the lower density of states regime before slowing than the corresponding $2.5E_g$ cohort. The proportion of excitons with energies above the $2.0E_g$ threshold can be seen in Figure 3.5.

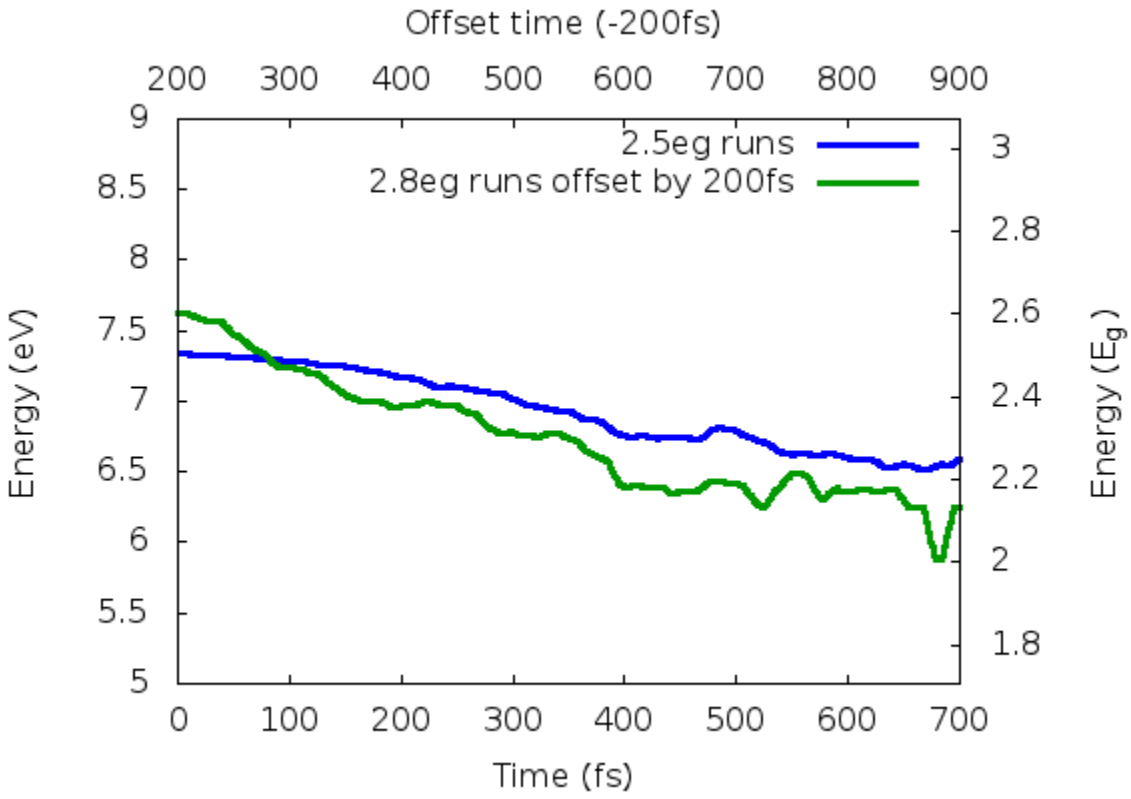

Figure 3.2: The average exciton energy vs. time curves for $Cd_{83}Se_{81}$ seen in Fig. 3.1 with the $2.8E_g$ initial exciton energy cohort shifted by -200fs to highlight convergent slopes at similar energies.

Once again, the slopes of the curves are qualitatively the same. Of note, the $2.8E_g$ initial energy cohort actually had trajectories decay faster below the energy threshold than the $2.5E_g$ counterpart. This further underscores the effects of temperature on the dynamics of the system, as will be discussed further below.

3.2 Dynamics of Exciton Relaxation

The character of the exciton relaxation in $Cd_{20}Se_{19}$ and $Cd_{83}Se_{81}$ follow similar patterns. One can qualitatively notice these patterns from Figures B.1-B.4 in the Appendix B, which show individual trajectories. In all of the bright initial excitonic states, the electron

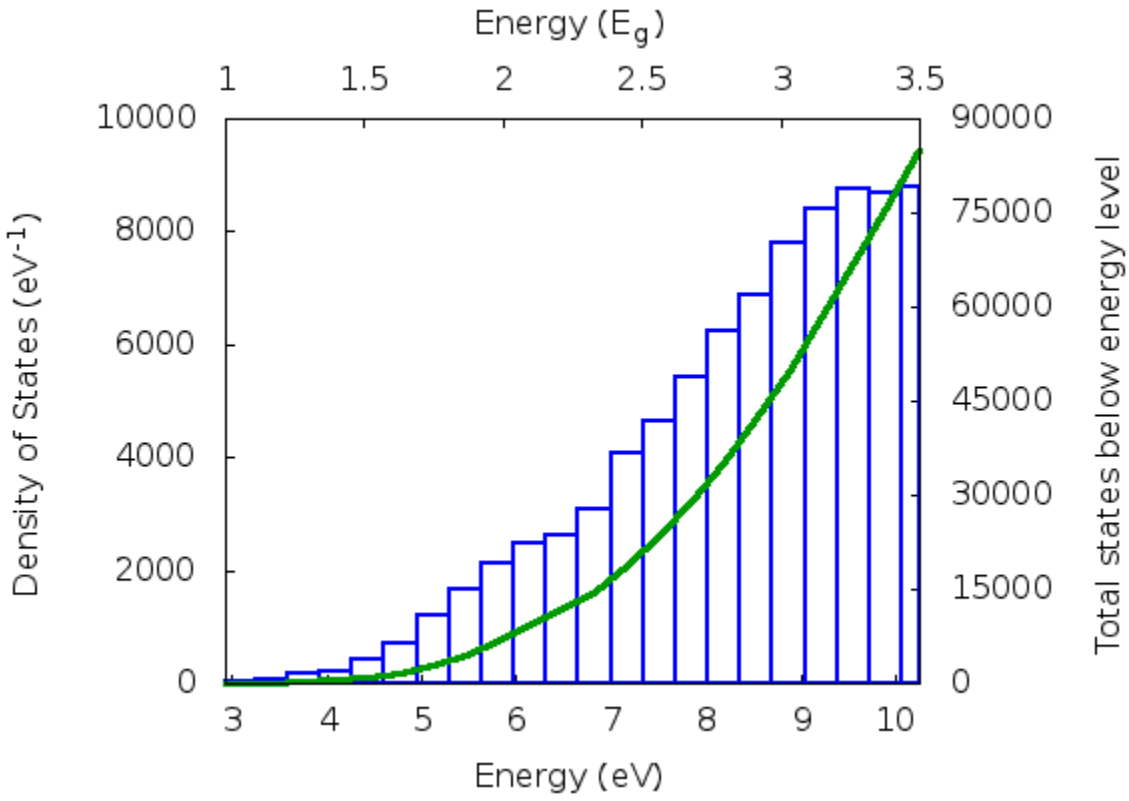

Figure 3.3: Density of exciton states with respect to energy for $Cd_{83}Se_{81}$. The green curve corresponds to the total number of exciton states that have an energy at or below the given energy. The boxes correspond to the number of excitonic states within each $0.1E_g$ bin.

was excited from an occupied orbital relatively close to the band edge. We observe that the electron undergoes a gradual decay punctuated by brief periods with a very rapid sequence of transitions. The hole follows a somewhat similar decay pathway upwards to the HOMO, though the periods of rapid transitions are less pronounced. This difference is mostly due to the fact that the holes starts within 1eV of the band edge in $Cd_{83}Se_{81}$ and within 2eV of the band edge in $Cd_{20}Se_{19}$.

Within the framework of Tully's fewest switches algorithm, the periods of rapid or large gap transitions appear as a single large "hop" [13]. The "hop" size distribution for the $2.8E_g$ cohort of $Cd_{83}Se_{81}$ trajectories are informative and can be found in Figure 3.6.

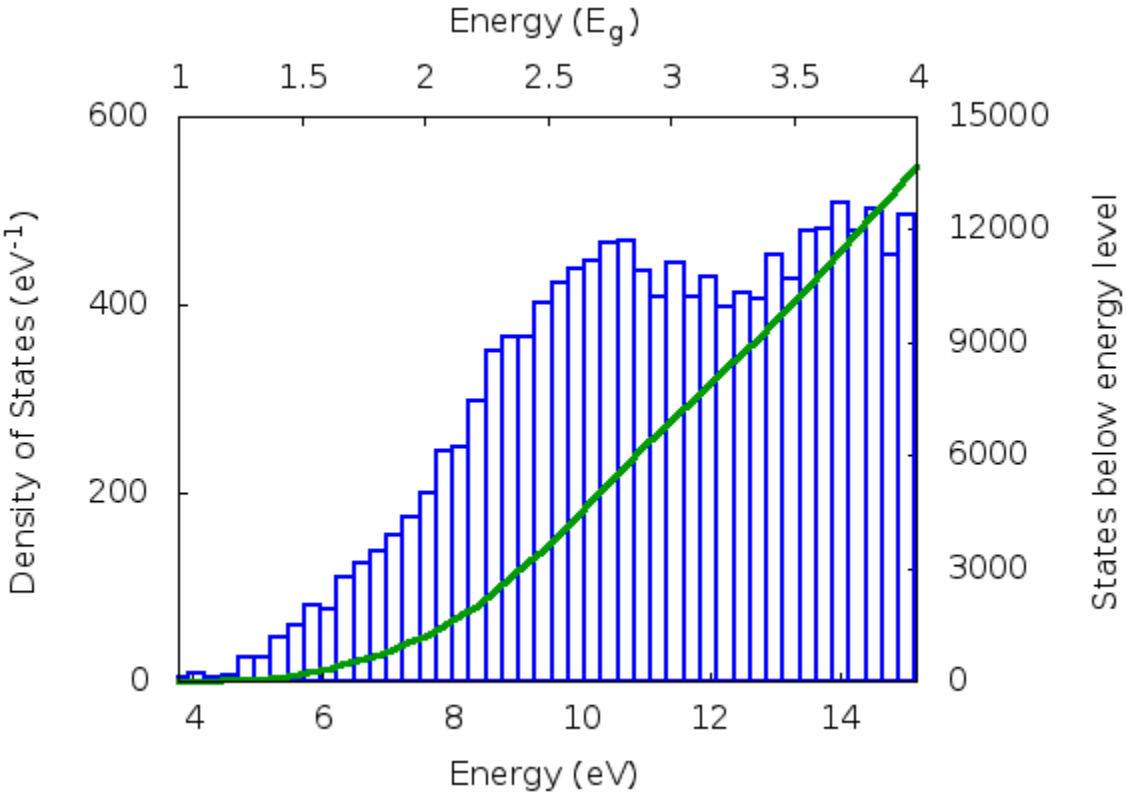

Figure 3.4: Density of exciton states with respect to energy for $Cd_{20}Se_{19}$. The green curve corresponds to the total number of exciton states that have an energy at or below the given energy. The boxes correspond to the number of excitonic states within each $0.1E_g$ bin.

The same plot for the $3.5E_g$ cohort of $Cd_{20}Se_{19}$ can be found in Figure 3.7. Corresponding plots for the remaining simulations can be found in the supplemental data, Figures B.5-B.7. These plots are all similar to the two shown.

Looking at Figures 3.6 and 3.7, the vast majority of transitions are between closely neighbouring states. However, the number of downward transitions of this size do not significantly outnumber upward transitions. A large portion of these ± 1 transitions are a result of back-and-forth "bouncing" between neighbouring states. This trend is more pronounced in the hole relaxation. The lower number of states within the valence band allows the strong nonadiabatic couplings between some of the neighbouring states to influence the dynamics

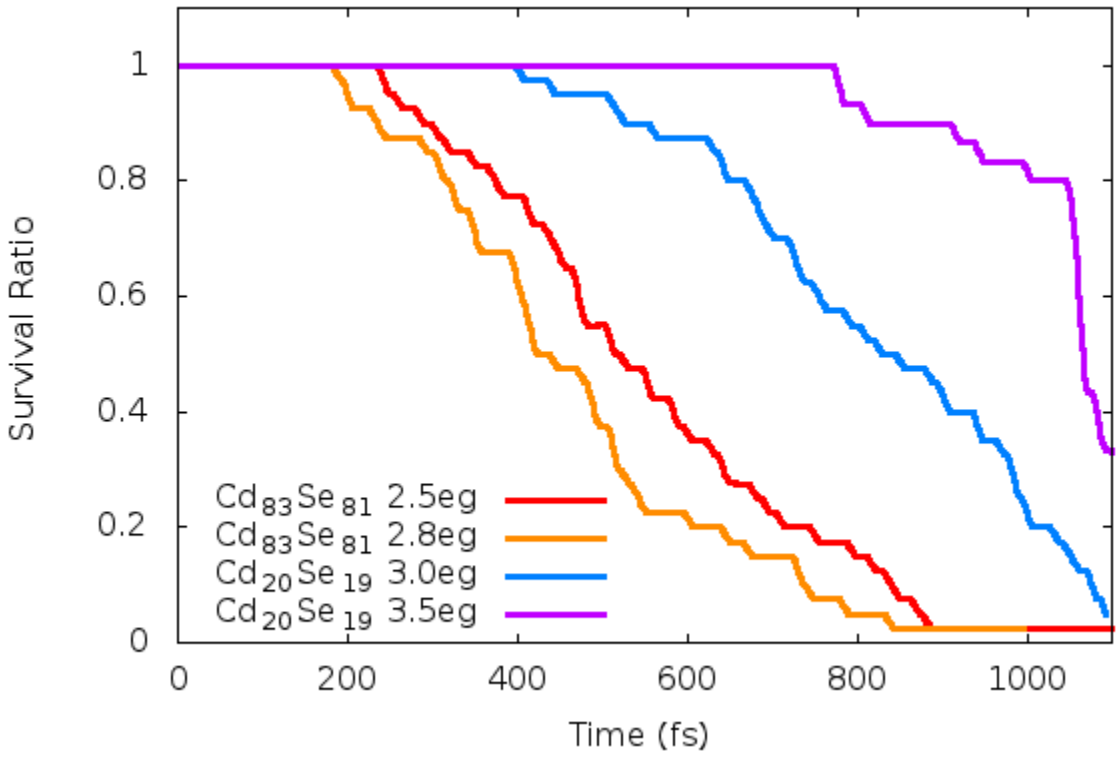

Figure 3.5: Simulated surviving fraction of excitons with exciton energy greater than $2.0E_g$. The $4.0E_g$ cohort of $Cd_{20}Se_{19}$ is not shown; the shortest decay time observed exceeds 1ps.

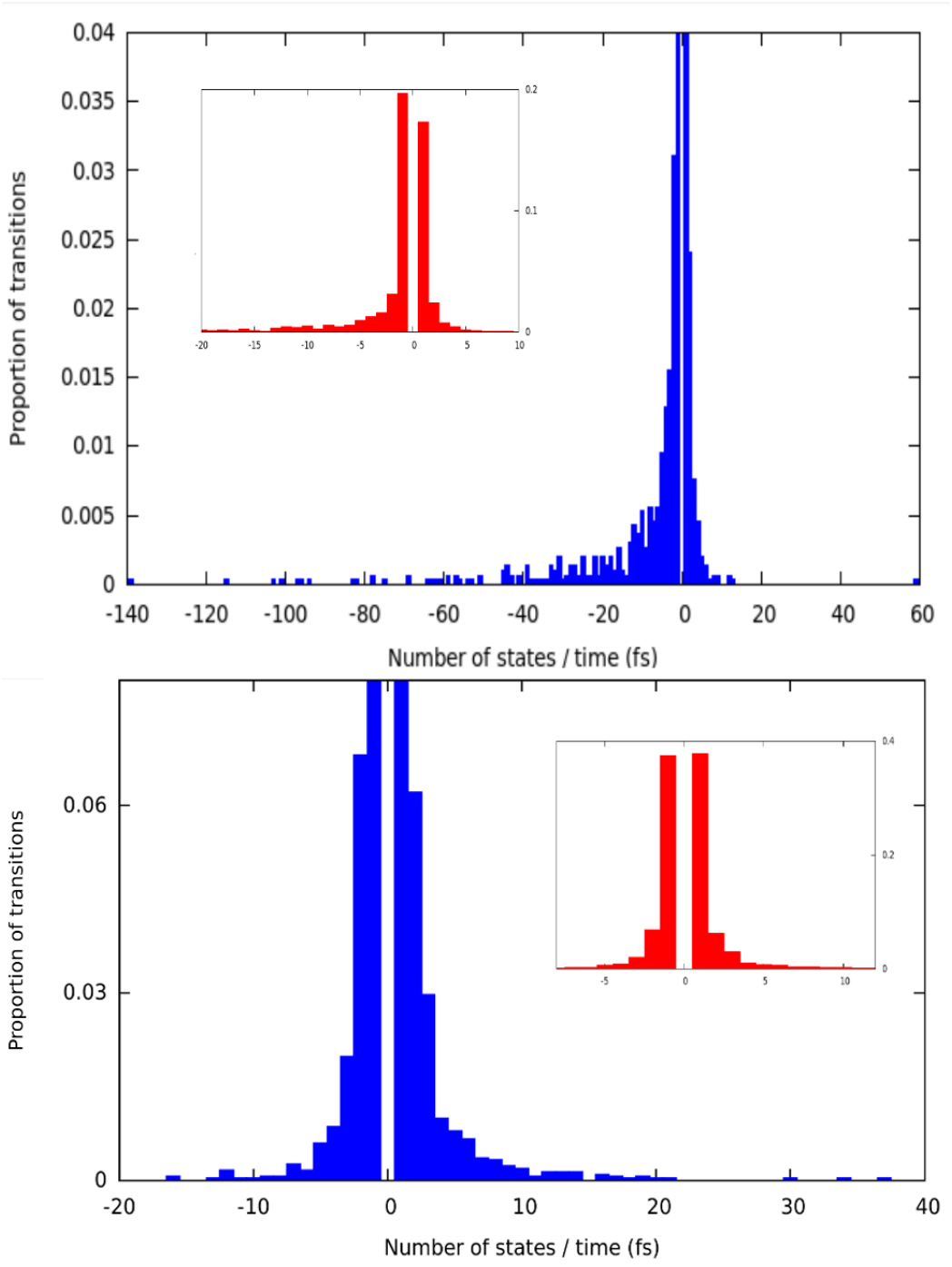

Figure 3.6: Distribution of hop sizes in absolute number of hole states (top) and virtual electron states (bottom) for $2.8E_g$ initial exciton energy cohort of $Cd_{83}Se_{81}$ trajectories. The image has been truncated vertically in order to better visualize the tails of the distribution. The non-truncated image can be seen in the inset.

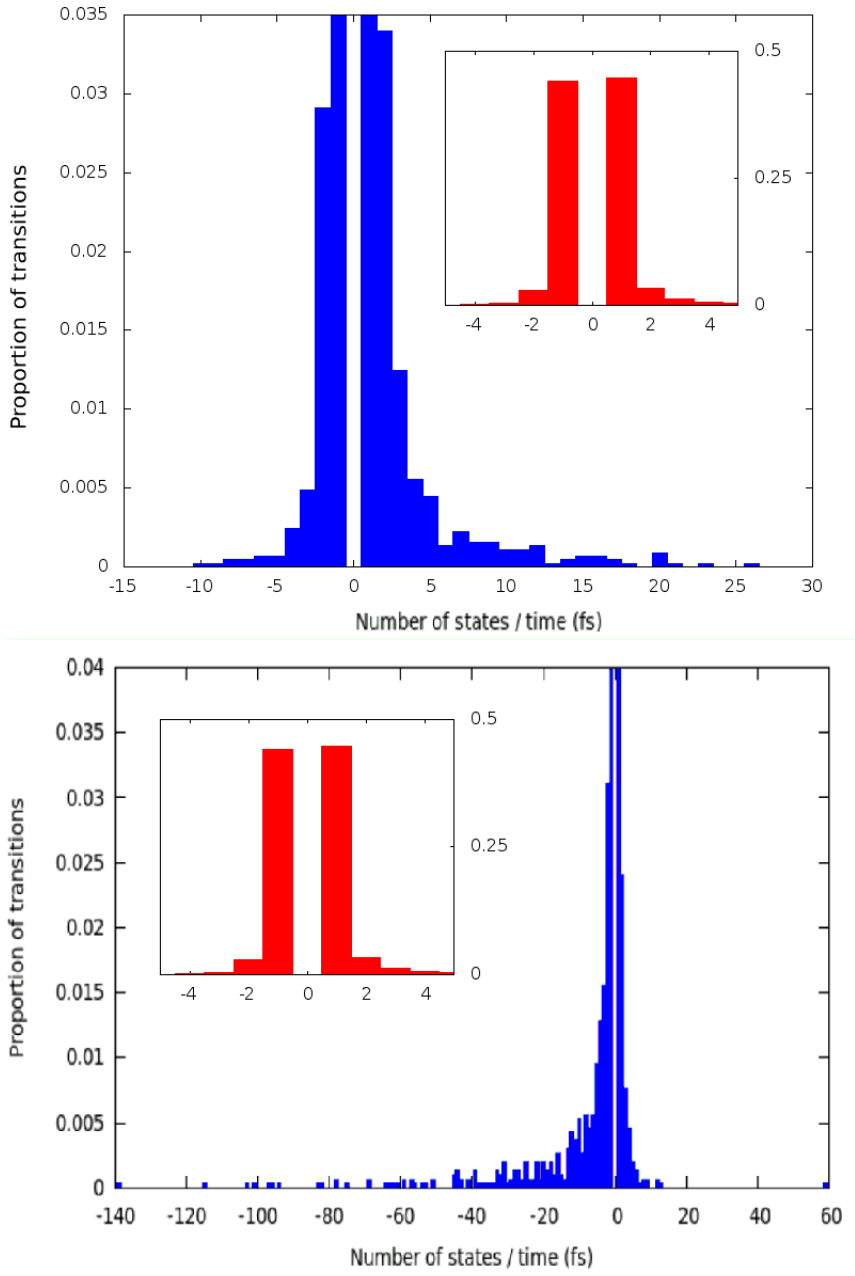

Figure 3.7: Distribution of hop sizes in absolute number of hole states (top) and virtual electron states (bottom) for $3.5E_g$ initial exciton energy cohort of $Cd_{20}Se_{19}$ trajectories. The image has been truncated vertically to better visualize the tails of the distribution. The non-truncated image can be seen in the inset.

to a greater degree.

A significant portion of the exciton energy is transferred to the classical coordinates through a handful of large, low-probability transitions. There is an approximately 200fs delay before these states are significantly populated. Clearly, there must be adequate nonadiabatic coupling between states to motivate such a transition. The magnitude of the square of the nonadiabatic couplings (equation 2.25) are considered in Figures 3.8 and 3.9. There are non-negligible couplings between widely separated states that allow these large transitions to occur.

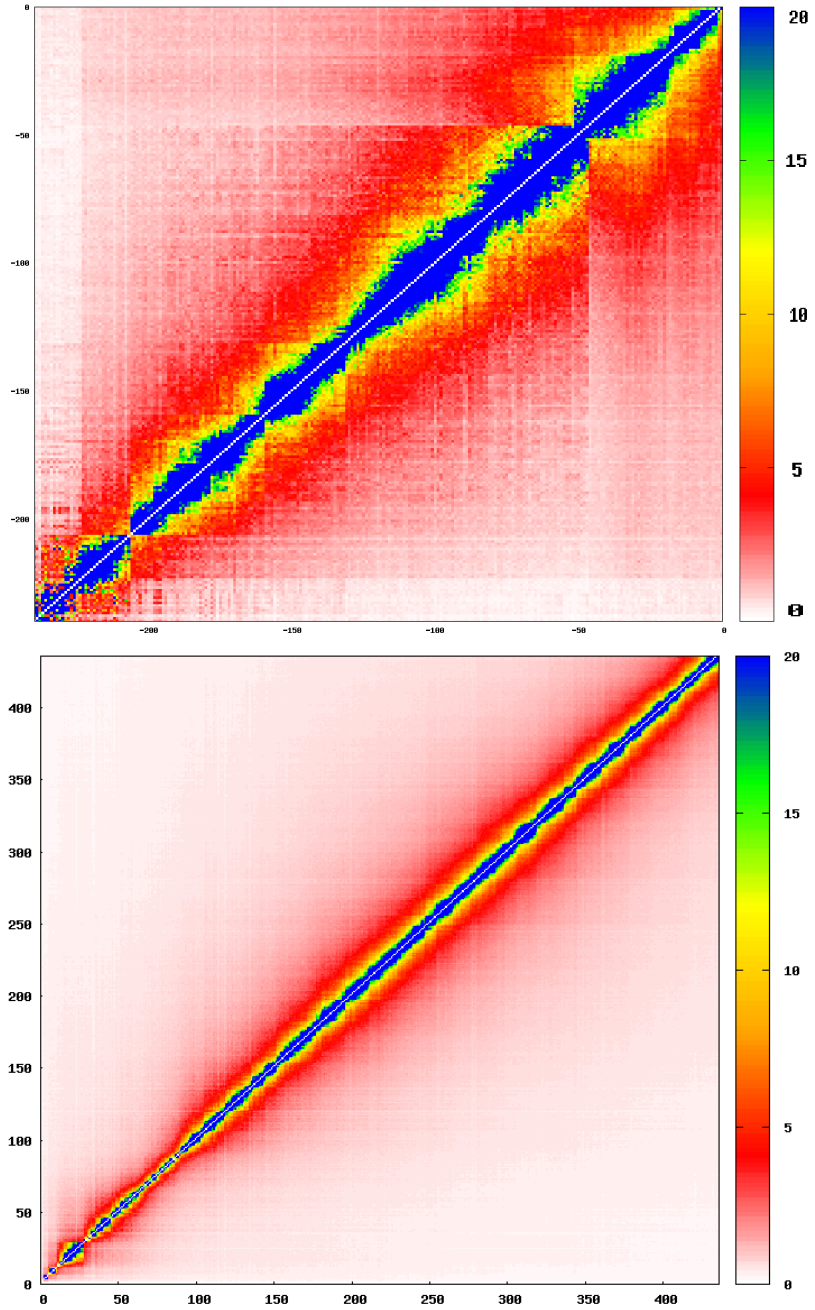

Figure 3.8: The square of the nonadiabatic couplings between hole states (top) and between electron states (bottom) for $Cd_{83}Se_{81}$. The color legend has been truncated so detail can be viewed. The non-truncated plots can be found in Appendix B. The maximum reaches 48000 for hole states and 31000 for electron states

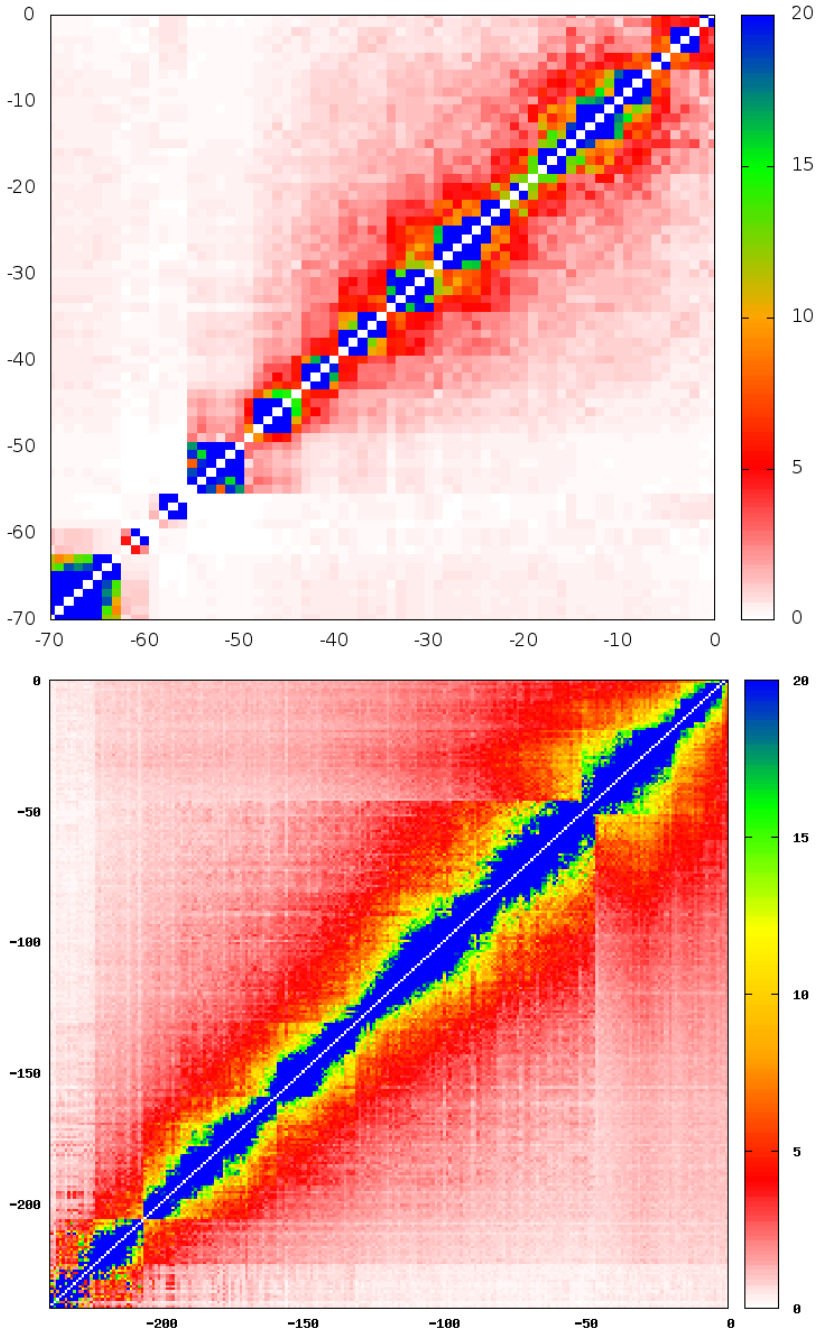

Figure 3.9: The square of the nonadiabatic couplings between hole states (top) and between electron virtual states (bottom) for $Cd_{20}Se_{19}$. The color legend has been truncated so detail can be viewed. The non-truncated plots can be found in Appendix B. The maximum reaches 7800 for hole states and 680 for electrons states.

Chapter 4

Conclusions

We have simulated singlet exciton decay in $Cd_{20}Se_{19}$ and $Cd_{83}Se_{81}$ using MDQT and Rabani's model for CdSe [12]. The simulations were initiated at 300K and with exciton energies in the 2.5-4.0E_g energy range. The exciton cooling seen in $Cd_{20}Se_{19}$ and $Cd_{83}Se_{81}$ simulations was on the order of 1ps and exhibited a dependence on the exciton density of states and the temperature of the cluster. These factors seemed to generally balance each other out, as evidenced by the relatively consistent rate of relaxation across both cluster sizes and the initial exciton energy ranges. The time needed for an exciton to relax below 2.0E_g, the point where Multiple Exciton Generation is no longer possible, is highly dependent on the initial exciton energy.

The exciton relaxation seems to follow a gradual pattern of decay punctuated by brief and intermittent periods of rapid relaxation. In both clusters, the average rates of exciton cooling slowed as the number of lower-laying states rapidly drops off near the 2.0E_g cutoff. The rate of exciton relaxation also appeared to increase with temperature, raising the values for the nonadiabatic couplings between states.

Other structures were not modelled in this study. The large number of exciton states and the full matrix of off-diagonal Hamiltonian terms led to memory and CPU time constraints. The memory constraints were the most problematic for $Cd_{83}Se_{81}$ due to its higher density of states. The increase in the density of states with cluster size does outweigh the decrease in the band gap with increasing size. Large-memory computer systems would in principle be able to model larger clusters, such as $Cd_{151}Se_{147}$ and $Cd_{232}Se_{251}$. Analogous

pair potentials and electronic pseudopotentials already exist for zinc-blende CdSe nanoparticles, so these systems would be a natural extension for this study [1, 12]. Additionally, this model could be applied to several other II-VI semiconducting nanocrystals, such as InAs [8].

Appendices

Appendix A

Singlet-Singlet Coupling Elements

In this section, the coupling terms will be defined. Much of the mathematical framework is based on the "Many Electron Wave Functions and Operators" chapter of Szabo and Ostlund's *Modern Quantum Chemistry* book [17].

The ground electronic state is a determinant of occupied single electron basis functions, as defined by equation 2.9. Exciton determinants were defined in equation 2.11. Because the spin-orbitals are orthonormal, the determinant $|\Psi_a^r\rangle$ is orthogonal to $|\Psi_b^s\rangle$ for all $b \neq a$ and $r \neq s$ [17]. As a result,

$$\left\langle \Psi_a^r \middle| \Psi_{b\neq a}^r \right\rangle = \left\langle \Psi_a^r \middle| \Psi_a^{r\neq s} \right\rangle = \left\langle \Psi_a^r \middle| \Psi_{a\neq b}^{r\neq s} \right\rangle = 0. \tag{A.1}$$

Here, a, b refer to hole states, r, s refer to excited electron states, and i, j are generalized indexes.

As was discussed previously in Section **2.1.1** (equation 2.12), the electronic states studied were all defined as singlet states. This means that the particular coupling element $\langle i|O|j\rangle$ takes the form of

$$\langle {}^s\psi_a^r|O|{}^s\psi_b^s\rangle = \frac{1}{2}\left(\langle\psi_a^r| + \langle\psi_{\overline{a}}^{\overline{r}}|\right) O(|\psi_b^s\rangle + |\psi_{\overline{b}}^{\overline{s}}\rangle) \tag{A.2}$$

$$= \frac{1}{2}\left(\langle\psi_a^r|O|\psi_b^s\rangle + \langle\psi_a^r|O|\psi_{\overline{b}}^{\overline{s}}\rangle + \langle\psi_{\overline{a}}^{\overline{r}}|O|\psi_b^s\rangle + \langle\psi_{\overline{a}}^{\overline{r}}|O|\psi_{\overline{b}}^{\overline{s}}\rangle\right). \tag{A.3}$$

Because there is no direct difference between the spin-up and spin-down states within the model in use, the first and fourth terms in equation A.3 are identical to each other. The same applies to the second and third terms. The spin states only affect the final form of the

electronic couplings. The final result can then be written matching spin and non-matching spin terms:

$$\langle {}^s\psi_a^r|O|{}^s\psi_b^s\rangle = \frac{1}{2}(2\langle\psi_a^r|O|\psi_b^s\rangle + 2\langle\psi_a^r|O|\psi_{\overline{b}}^{\overline{s}}\rangle). \tag{A.4}$$

A.1 Nonadiabatic Coupling

The nonadiabatic coupling vector is defined generally in equation 2.25 and more specifically in equation 2.33. Because the overlap between two state determinants is zero if $a \neq b$ *or* $r \neq s$ and the $\nabla_{\mathbf{R}}$ operator can only operate on one state, $\mathbf{d}_{ij} = 0$ if two state determinants differ by more than one term. For example, consider $\langle\psi_a^r|\mathbf{d}|\psi_{\overline{a}}^{\overline{r}}\rangle$. The two determinants, in maximum coincidence are:

$$|\psi_a^r\rangle = |\cdots\chi_r\chi_{\overline{a}}\cdots\rangle$$

$$|\psi_{\overline{a}}^{\overline{r}}\rangle = |\cdots\chi_a\chi_{\overline{r}}\cdots\rangle$$

Substituting these determinants into 2.33, we obtain:

$$\langle {}^s\psi_a^r(\mathbf{r};\mathbf{R})|\nabla_{\mathbf{R}}\,{}^s\psi_{\overline{a}}^{\overline{r}}(\mathbf{r};\mathbf{R})\rangle = \sum_\alpha \frac{\langle\chi_r\chi_{\overline{a}}|\nabla_{\mathbf{R}}v_\alpha(\mathbf{r}-\mathbf{R})|\chi_a\chi_{\overline{r}}\rangle}{\epsilon_j - \epsilon_i}, \tag{A.5}$$

which, written out becomes

$$\sum_\alpha \frac{\langle\chi_r\chi_{\overline{a}}|\nabla_{\mathbf{R}}v_\alpha(\mathbf{r}-\mathbf{R})|\chi_a\chi_{\overline{r}}\rangle}{\epsilon_j - \epsilon_i}$$
$$= \frac{1}{\epsilon_j - \epsilon_i}\sum_\alpha \left(\int \chi_r^*(\mathbf{x}_1)\nabla_{\mathbf{R}}v_\alpha(\mathbf{r}_1-\mathbf{R})\chi_a(\mathbf{x}_1)d\mathbf{x}_1\right)\int \chi_{\overline{a}}^*(\mathbf{x}_2)\chi_{\overline{r}}(\mathbf{x}_2)d\mathbf{x}_2 = 0. \tag{A.6}$$

As can be seen in the right-hand integral, $\nabla_{\mathbf{R}}v_\alpha(\mathbf{r}_1 - \mathbf{R})$ does not affect coordinate x_2. Since we use an orthonormal basis, this integral has a zero value. This will be the case any time the two determinants in question differ by more than one term. Additionally, if $\langle\phi_i|\phi_i\rangle = 1$, taking the gradient of ϕ_i with respect to $\mathbf{R}$, like in equation 2.25, results in $\langle\phi_i|\nabla_{\mathbf{R}}|\phi_i\rangle = 0$.

It should also be noticed that there is no way to have the spin-up and spin-down determinants to differ by less than two terms. In this sense, only the spin-matching case in equation A.4 has a non-zero value.

The last feature to discuss with respect to $\mathbf{d}_{ij}$ is the situation in which the two spin determinants in question have the same excited electron state. A perturbation can bring the two determinants into maximum coincidence as below.

$$|\psi_a^r\rangle = |\cdots \chi_r \chi_{\overline{a}} \cdots \chi_b \chi_{\overline{b}} \cdots\rangle \tag{A.7a}$$

$$|\psi_b^r\rangle = |\cdots \chi_a \chi_{\overline{a}} \cdots \chi_r \chi_{\overline{b}} \cdots\rangle = -|\cdots \chi_r \chi_{\overline{a}} \cdots \chi_a \chi_{\overline{b}} \cdots\rangle \tag{A.7b}$$

This negative 1 carries through the calculation. These two determinants now differ by one term. In summation,

$$\sum_\alpha \langle {}^s\psi_a^r | \nabla_{\mathbf{R}} v_\alpha(\mathbf{r}-\mathbf{R}) | {}^s\psi_b^s\rangle = \sum_\alpha \left(\frac{1}{\epsilon_r - \epsilon_s} \langle \chi_r | \nabla_{\mathbf{R}} v_\alpha | \chi_s \rangle \delta_{ab} - \frac{1}{\epsilon_a - \epsilon_b} \langle \chi_a | \nabla_{\mathbf{R}} v_\alpha | \chi_b \rangle \delta_{rs} \right) \tag{A.8}$$

where δ_{ab} is the Kronecker delta function for a and b. Using a single index for each exciton state, we obtain the definition for $\mathbf{d}_{ij}$ seen in equation 2.25.

A.2 Off-diagonal Coulomb Couplings

As discussed in Section **2.2**, the off diagonal coulomb couplings, V_{ij}, are defined by 2.24. Again, the off-diagonal elements of the Hamiltonian reduce to the element of U, which is defined in equation 2.6. This is the two-electron term minus the H_1 coulomb and exchange terms (J_1 and K_1, respectively) found in equation 2.6.

These one-electron J and K terms between general states j and k operating on spin-orbital χ_j can be expressed as

$$J_k(\mathbf{x}_1)\chi_j(\mathbf{x}_1) = \left(\int d\mathbf{x}_2 \chi_k^*(\mathbf{x}_2) r_{12}^{-1} \chi_k(\mathbf{x}_2) \right) \chi_j(\mathbf{x}_1) \tag{A.9}$$

and

$$K_k(\mathbf{x}_1)\chi_j(\mathbf{x}_1) = \left(\int d\mathbf{x}_2 \chi_k^*(\mathbf{x}_2) r_{12}^{-1} \chi_j(\mathbf{x}_2) \right) \chi_k(\mathbf{x}_1). \tag{A.10}$$

Since these one-electron coulomb and exchange terms are one-electron operators, they follow the same general rules as the nonadiabatic coupling vector discussed in the previous section. These operators are zero if the two spin-determinants differ by more than one term. Therefore, these operators do not directly couple states with opposing spin. The only difference between these operators and the nonadiabatic coupling vector is the diagonal terms are not zero. The results of J_k and K_k operating of state χ_k is

$$J_k(\mathbf{x}_1)\chi_k(\mathbf{x}_1) = \sum_i \left(\int d\mathbf{x}_2 \chi_k^*(\mathbf{x}_2) r_{12}^{-1} \chi_k(\mathbf{x}_2) \right) \chi_i(\mathbf{x}_1) \tag{A.11}$$

and

$$K_k(\mathbf{x}_1)\chi_k(\mathbf{x}_1) = \sum_i \left(\int d\mathbf{x}_2 \chi_k^*(\mathbf{x}_2) r_{12}^{-1} \chi_i(\mathbf{x}_2) \right) \chi_k(\mathbf{x}_1). \tag{A.12}$$

The two-electron coulomb and exchange terms are simply:

$$\langle \chi_r \chi_a | W_2 | \chi_s \chi_b \rangle = v_{arbs} - v_{absr} \tag{A.13}$$

where the v_{ijkl} notation is defined previously in equation 2.30. Within our framework, these integrals can couple any two exciton states. The only non-obvious behavior of these integrals is that the exchange operator is zero in the case of opposing spins. Since the exchange operator exchanges electron coordinate x_1 and x_2, an overlap of opposing spin states occurs. Because of this, the exchange integrals for opposing spins is

$$v_{a\overline{b}s\overline{r}} = \int \int d\mathbf{x}_1 d\mathbf{x}_2 \chi_a^*(\mathbf{x}_1) \chi_{\overline{b}}(\mathbf{x}_1) r_{12}^{-1} \chi_{\overline{s}}^*(\mathbf{x}_2) \chi_r(\mathbf{x}_2) = 0. \tag{A.14}$$

Applying these results to equation A.4, we obtain the following results for $a \neq b$ *and* $r \neq s$:

$$\langle \chi_r \chi_a | W_2 | \chi_s \chi_b \rangle = 2v_{arbs} - v_{absr}. \tag{A.15}$$

Similarly, if the determinants differ by one term, such as if $a = b$,

$$\langle \chi_r \chi_a | W_2 | \chi_s \chi_a \rangle = \sum_j 2v_{jrjs} - v_{jjsr}. \tag{A.16}$$

Finally, the diagonal elements are

$$\langle \chi_r \chi_a | W_2 | \chi_r \chi_a \rangle = \sum_{ij} 2v_{jiji} - v_{jjii}. \tag{A.17}$$

When the two determinants differ by less than two terms, W_2 is functionally identical to J and K. The only difference between W_2 and $J - K$ is that the opposing-spin coulomb term in equation A.4 is non-zero. The results of $W_2 - (J - K)$ are summarized in Table A.1.

$\langle {}^s\Psi_a^r \vert U \vert {}^s\Psi_b^s \rangle$	$a = b$	$a \neq b$
$r = s$	v_{arar}	v_{arbr}
$r \neq s$	v_{aras}	$2v_{arbs} - v_{absr}$

Table A.1: Elements of $U = W_2 - (J_1 - K_1)$ for different combinations of excitonic determinants. The notation for the integral v_{ijkl} is defined in equation 2.30.

Appendix B

Supplemental Data

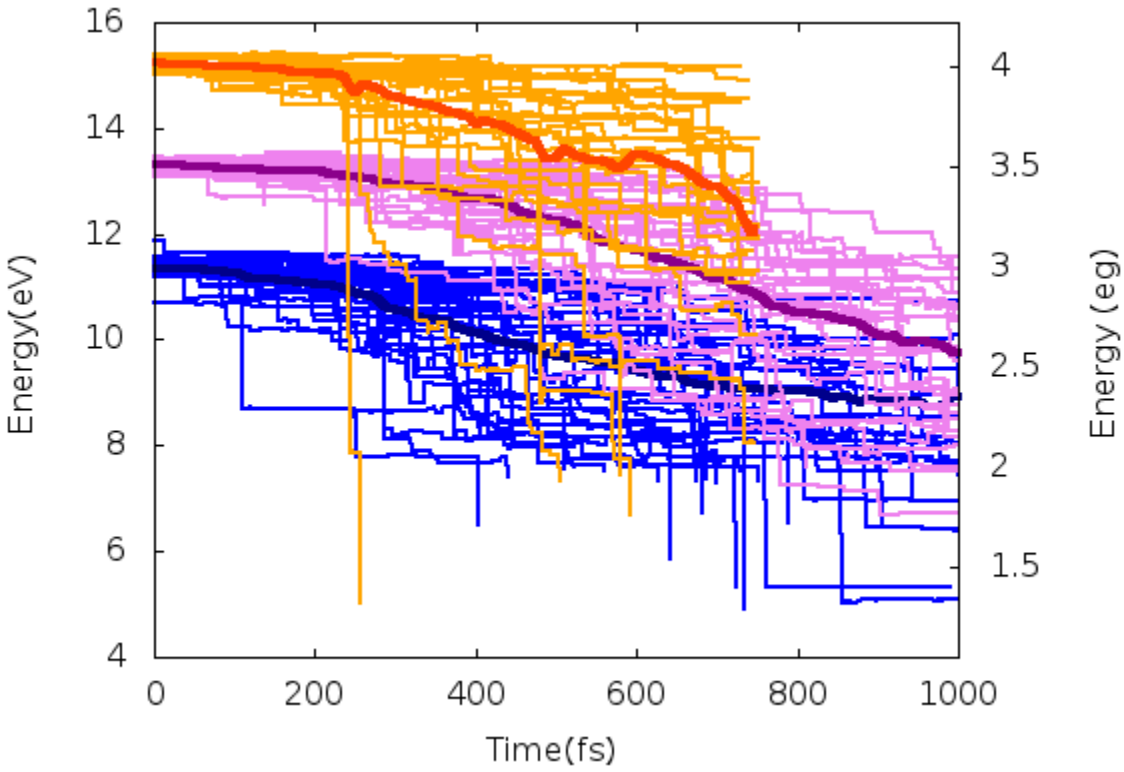

Figure B.1: Individual electronic trajectories for $Cd_{20}Se_{19}$. The top group ($4.0E_g$ initial exciton energy) ends early due to simulation wall clock limits. Thicker lines correspond to average energy of surviving excitons within that cohort, the same shown in Figure 3.1.

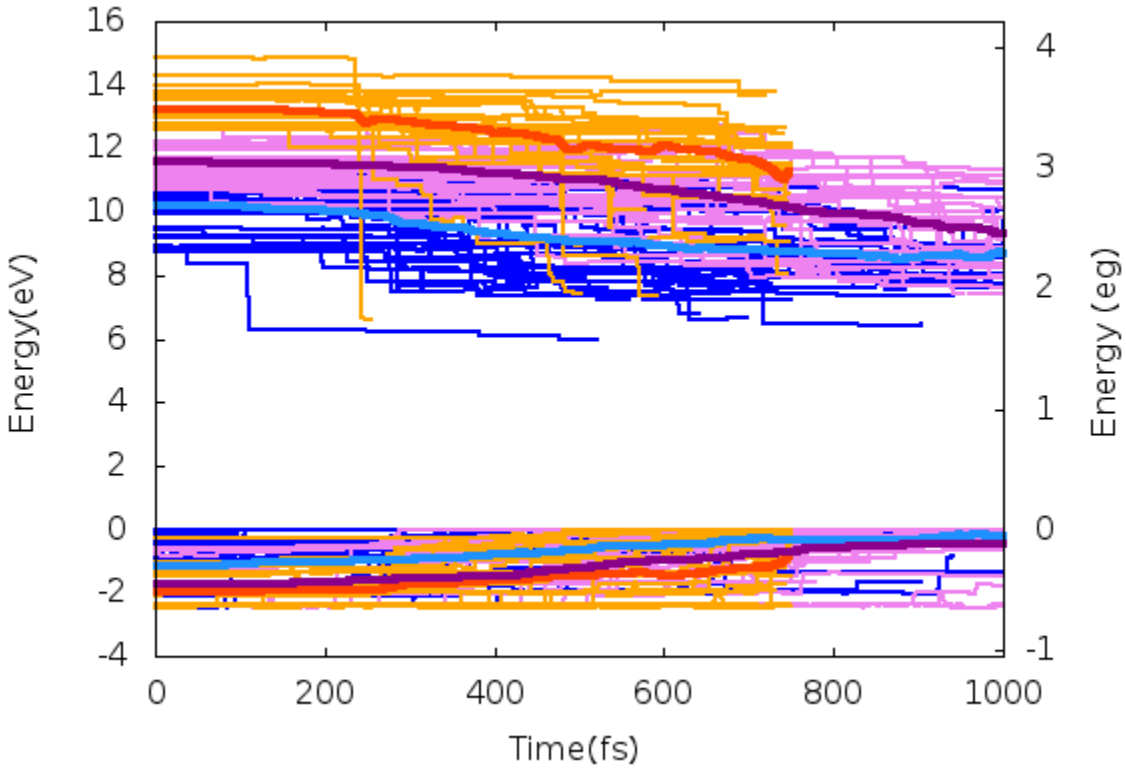

Figure B.2: Individual electronic trajectories for $Cd_{20}Se_{19}$ with electron and hole trajectories separated.

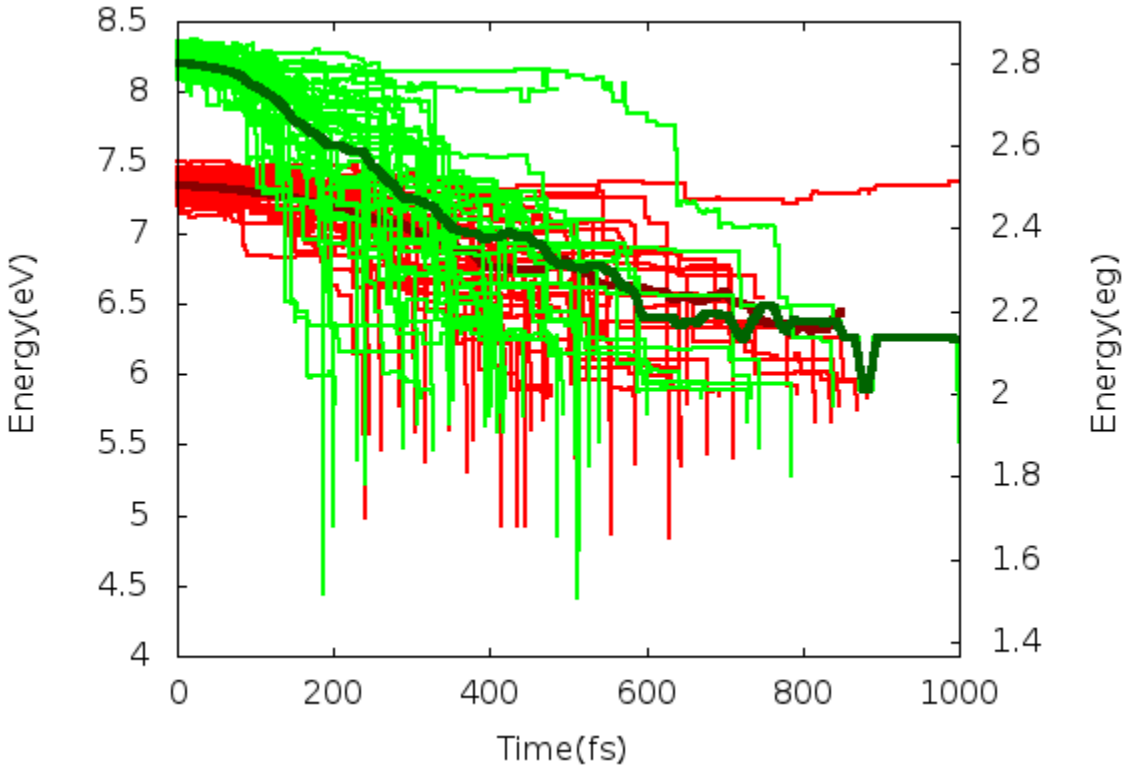

Figure B.3: Individual electronic trajectories for $Cd_{83}Se_{81}$.The thicker lines correspond to the average energy of surviving excitons within that cohort, the same shown in Figure 3.1.

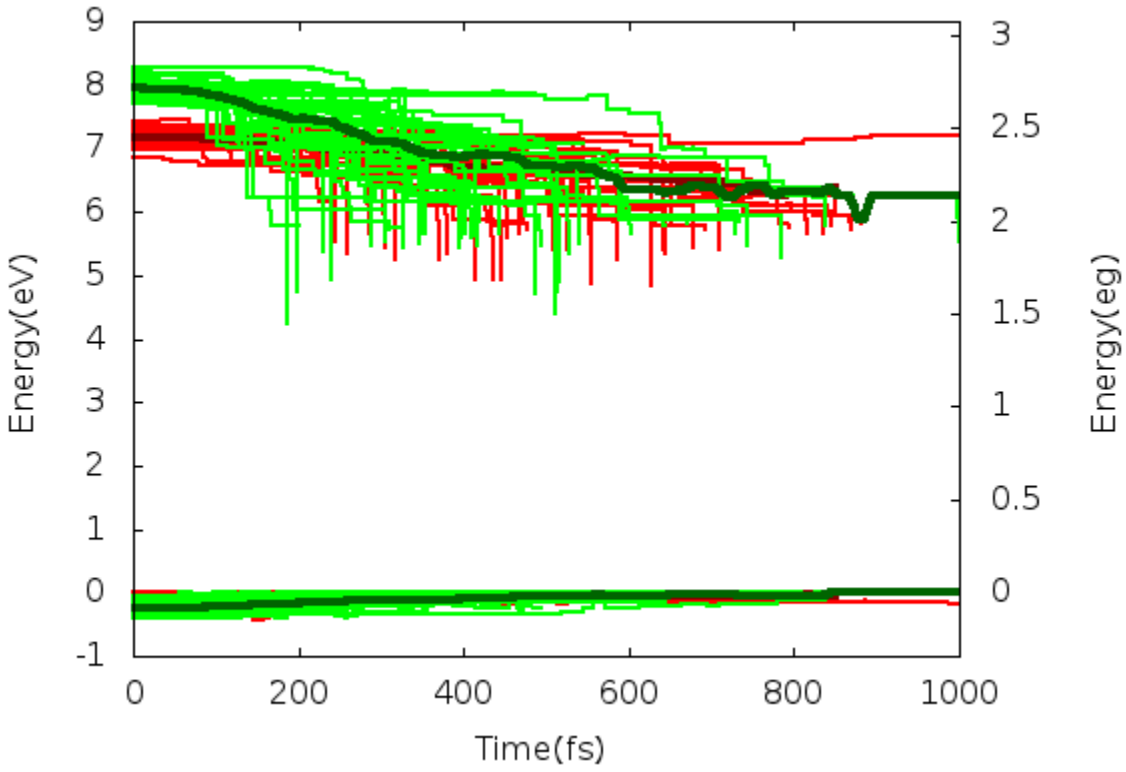

Figure B.4: Individual electronic trajectories for $Cd_{83}Se_{81}$ with electron and hole trajectories separated.

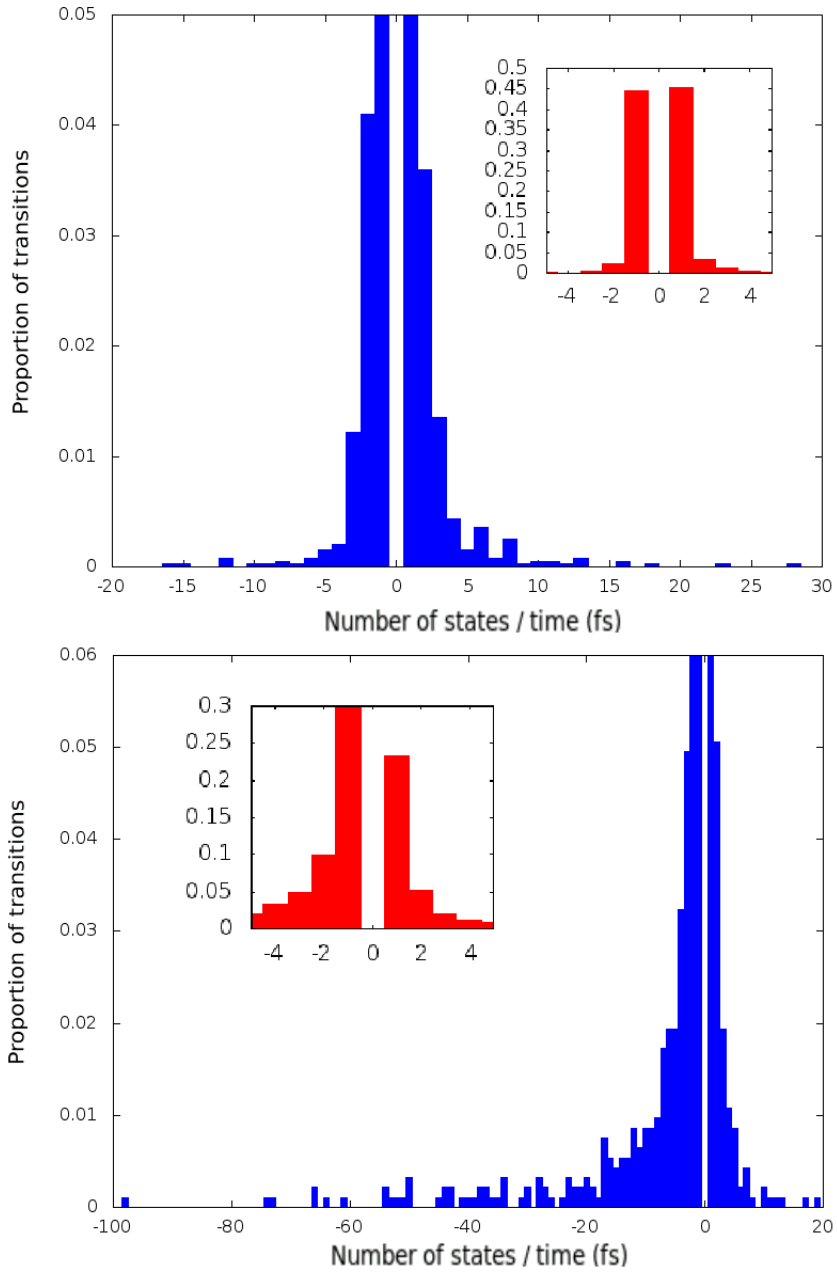

Figure B.5: Distribution of hop sizes in absolute number of hole states(top) and virtual electron states (bottom) for $2.5E_g$ initial exciton energy cohort of $Cd_{83}Se_{81}$ trajectories. The image has been truncated vertically order to better visualize the tails of the distribution. The unscaled image can be seen in the inset.

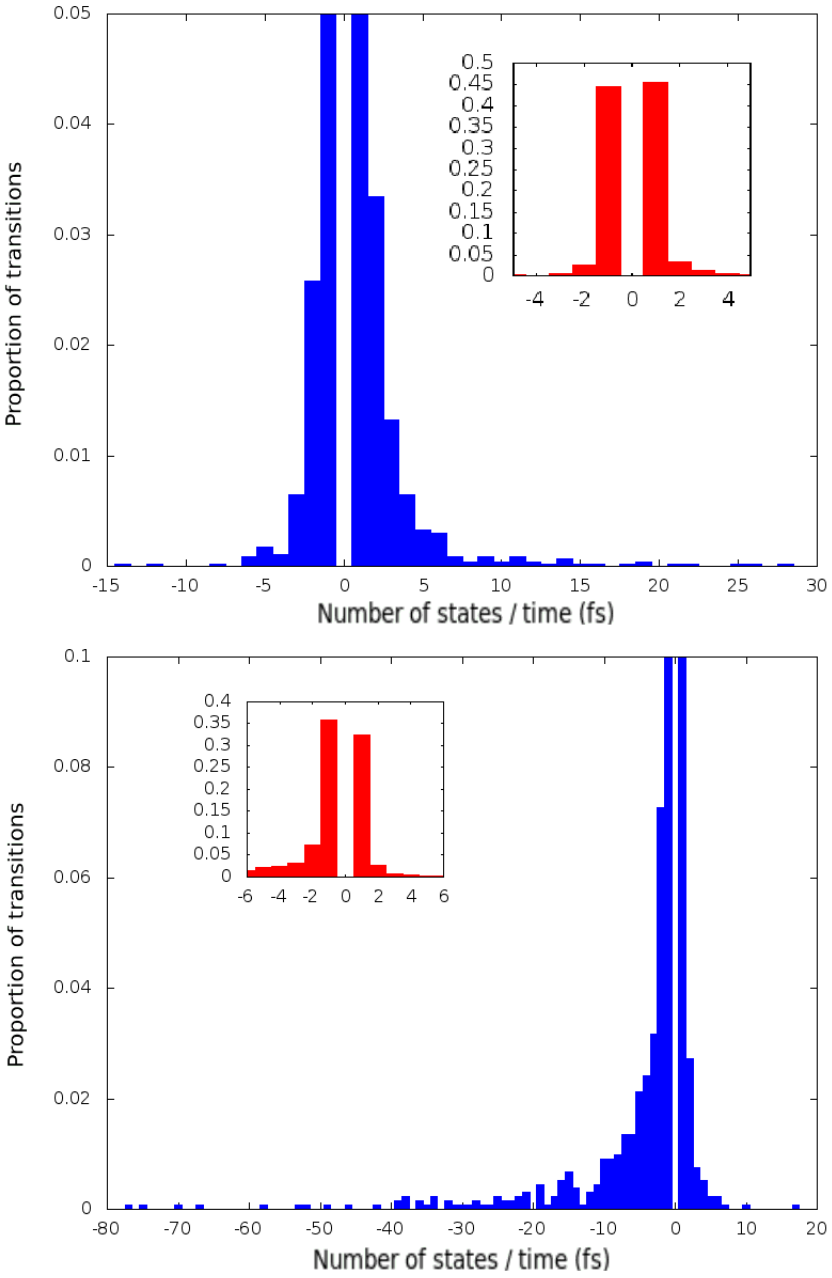

Figure B.6: Distribution of hop sizes in absolute number of hole states (top) and virtual electron states (bottom) for $3.0E_g$ initial exciton energy cohort of $Cd_{20}Se_{19}$ trajectories. The image has been truncated vertically to better visualize the tails of the distribution. The non-truncated image can be seen in the inset.

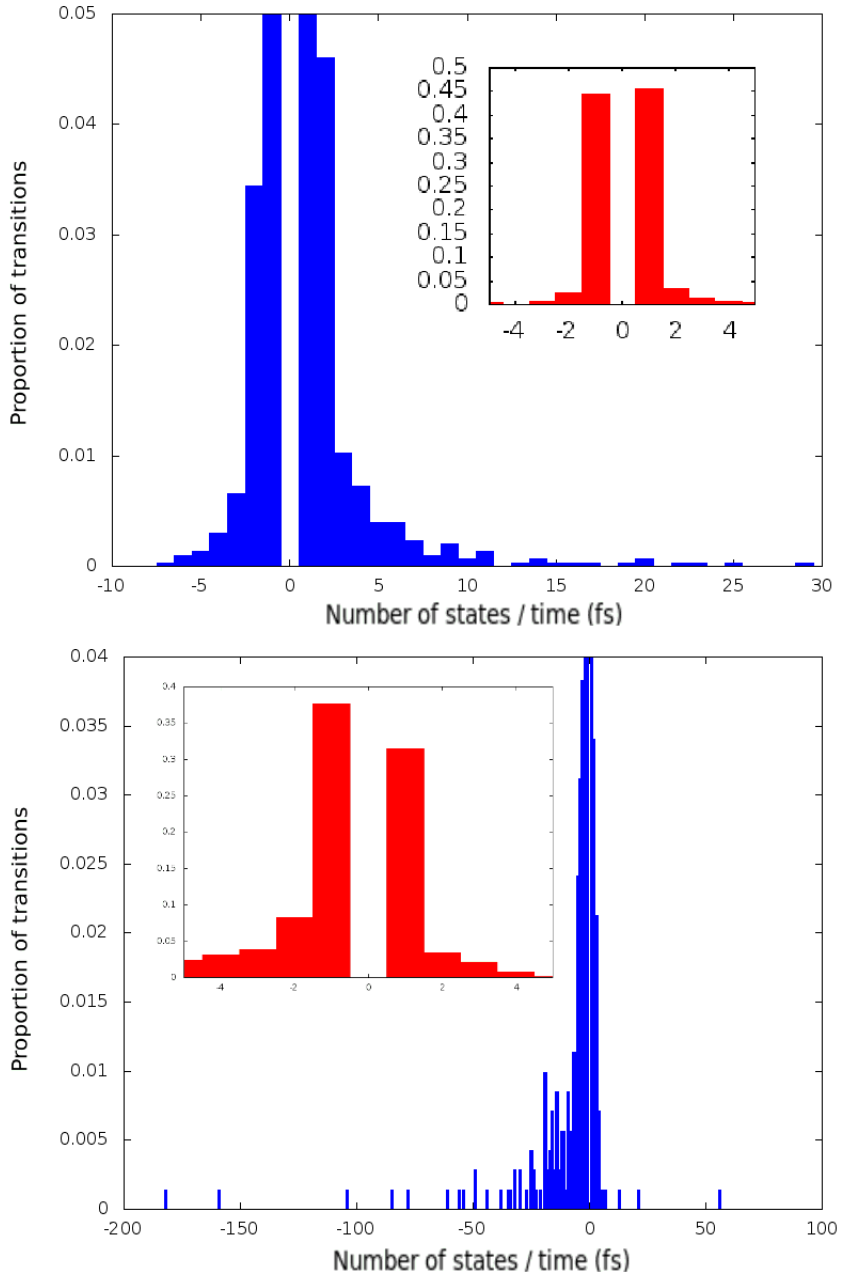

Figure B.7: Distribution of hop sizes in absolute number of hole states (top) and virtual electron states (bottom) for $4.0E_g$ initial exciton energy cohort of $Cd_{20}Se_{19}$ trajectories. The image has been truncated vertically to better visualize the tails of the distribution. The non-truncated image can be seen in the inset.

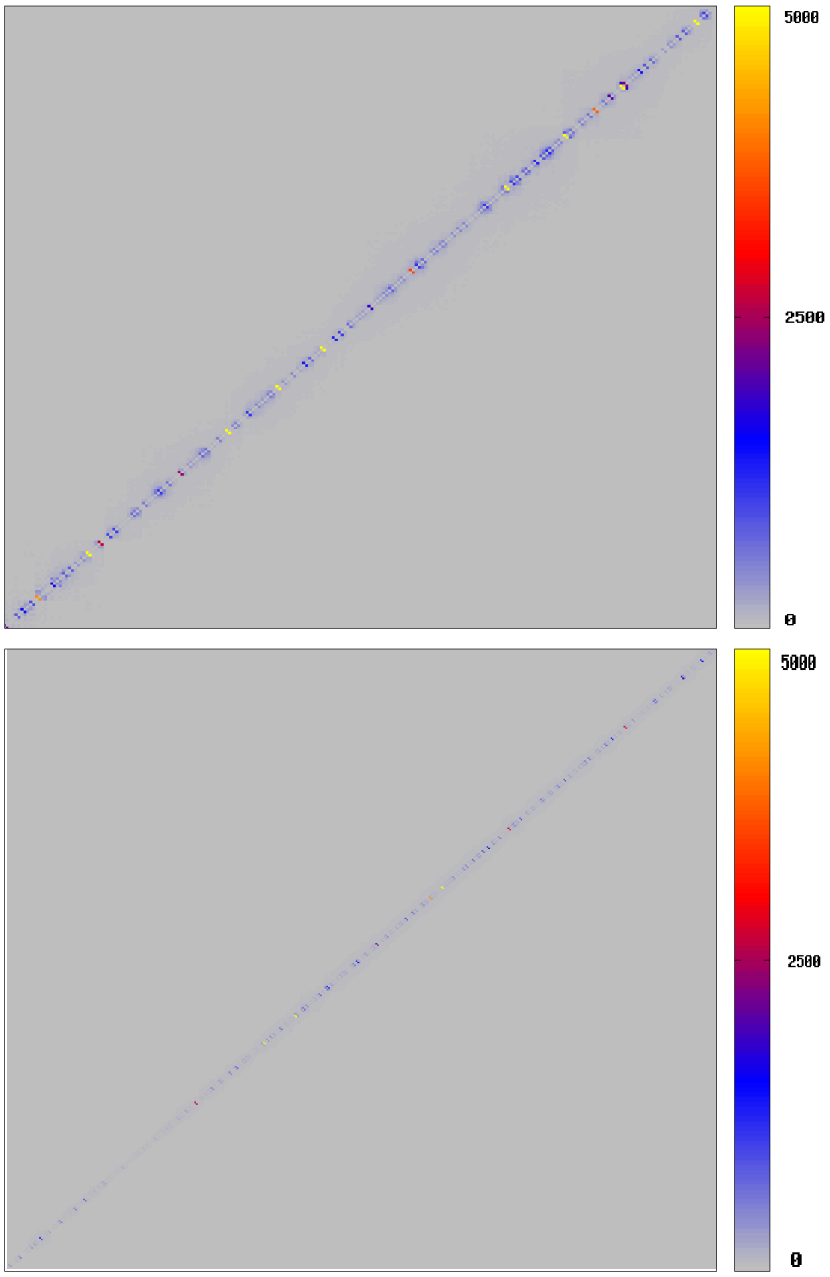

Figure B.8: The square of the nonadiabatic couplings between hole states (top) and electron virtual states (bottom) for $Cd_{83}Se_{81}$. This is the same data seen in Figure 3.8, though the key now spans the entire range of d^2 to highlight the strong coupling between nearby states.

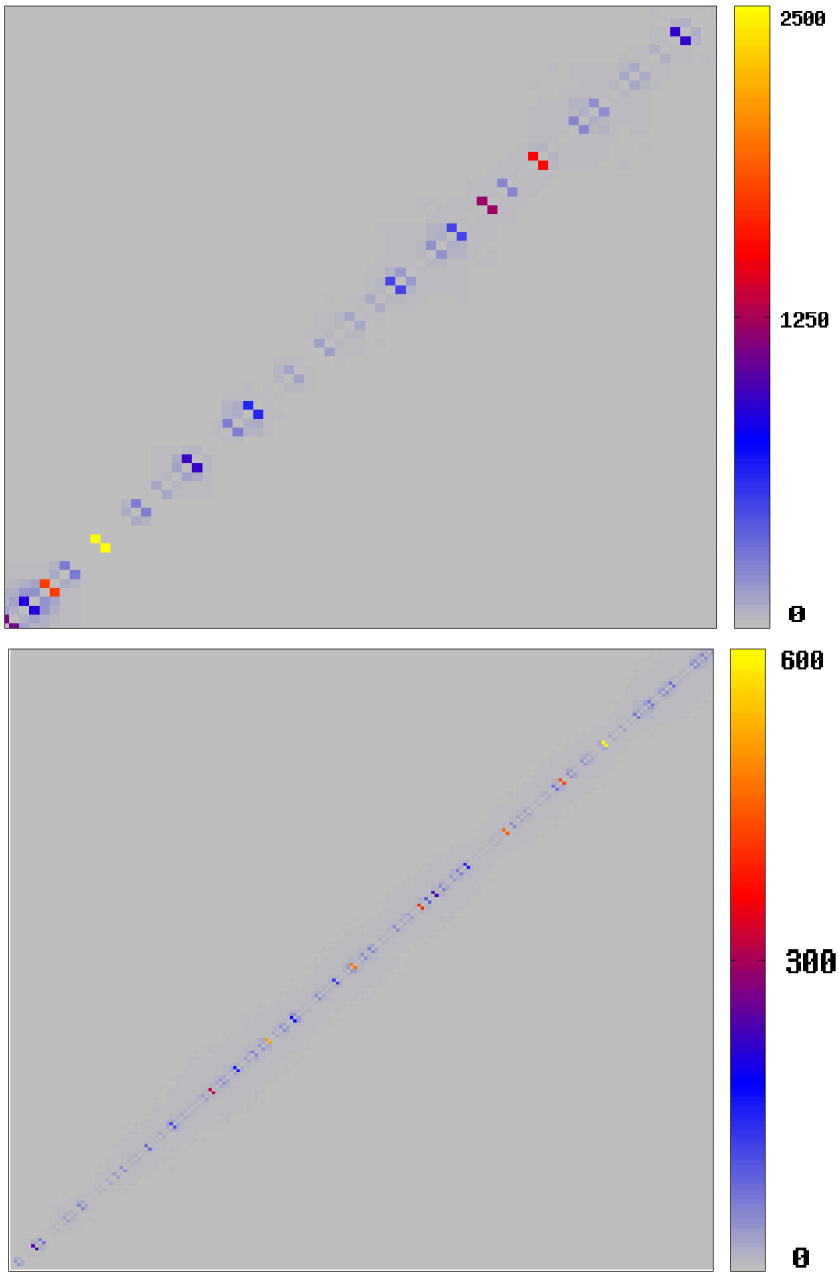

Figure B.9: The square of the nonadiabatic couplings between hole states (top) and electron virtual states (bottom) for $Cd_{20}Se_{19}$. This is the same data seen in Figure 3.9, though the key now spans the entire range of d^2 to highlight the strong coupling between nearby states.

Bibliography

[1] Rabani, E. *Journal of Chemical Physics* **116**(1), 258–262 JAN 1 (2002).

[2] Nozik, A. J. and Beard, M. C. and Luther, J. M. and Law, M. and Ellingson, R. J. and Johnson, J. C. *Chemical Reviews* **10**(11), 6873–6890 (2010).

[3] Alivisatos, A. P. *Science* **271**(5251), pp. 933–937 (1996).

[4] Huynh, W. U., Dittmer, J. J., and Alivisatos, A. P. *Science* **295**, 2425–2427 (2002).

[5] Hyeon-Deuk, K. and Prezhdo, O. V. *ACS Nano* **6**(2), 1239–1250 (2012).

[6] Shockley, W. and Queisser, H. J. *Journal of Applied Physics* **32**(3), 510–519 (1961).

[7] Alivisatos, A. P. *Journal of Physical Chemistry* **100**(31), 13226–13239 (1996).

[8] Rabani, E. and Baer, R. *CHEMICAL PHYSICS LETTERS* **496**(4-6), 227–235 AUG 30 (2010).

[9] Luo, J.-W., Franceschetti, A., and Zunger, A. *NANO LETTERS* **8**(10), 3174–3181 OCT (2008).

[10] Lin, Z., Franceschetti, A., and Lusk, M. T. *ACS Nano* **5**(4), 2503–2511 (2011).

[11] Prezhdo, O. V. *Accounts of Chemical Research* **42**(12), 2005–2016 DEC (2009).

[12] Rabani, E., Hetenyi, B., Berne, B., and Brus, L. *Journal of Chemical Physics* **110**(11), 5355–5369 MAR 15 (1999).

[13] Tully, J. C. *Journal of Chemical Physics* **93**(2), 1061–1071 (1990).

[14] Hammes-Schiffer, S. and Tully, J. C. *Journal of Chemical Physics* **101**(2), 4657–4667 (1994).

[15] Rabani, E. *Journal of Chemical Physics* **115**(3), 1493–1497 (2001).

[16] Prezdo, O. V. and Rossky, P. J. *Journal of Chemical Physics* **107**(3), 825–834 (1997).

[17] Szabo, A. and Ostlund, N. S. *Modern Quantum Chemistry: Introduction to Advance Electronic Structure Theory.* Dover, (1996).

[18] Rabani, E. and Baer, R. *Nano Letters* **8**(12), 4488–4492 (2008).

[19] Press, W. H., Vettering, W. T., Teukolsky, S. A., and Flannery, B. P. *Numerical Recipes in Fortran 77.* Cambridge University Press, 2nd edition, (1992).

[20] Klimov, V. I. and McBranch, D. W. *Phys. Rev. Lett.* **80**, 4028–4031 May (1998).

Vita

Kevin David Anderson grew up in and around the Dallas/Ft. Worth area of Texas. He received the Bachelor of Science degree in Chemistry with honours at the University of Alabama at Tuscaloosa. He then started his graduate studies in Physical Chemistry at the University of Texas at Austin in August, 2009.

Contact email: kevin.anderson@utexas.edu

This thesis was typeset with LaTeX[†] by the author.

[†]LaTeX is a document preparation system developed by Leslie Lamport as a special version of Donald Knuth's TeX Program.